$LRRK2_{G2019S}$ acts as a dominant interfering mutant in the context of iron overload

Andres Goldman[1, 5] 0000-0002-0322-139X, Mai Nguyen[1, 5], Joel Lanoix[2, 5] 0000-0001-7073-9298, Ahmed Fahmy[3, 5] 0000-0003-0444-383X, Yong Zhong Xu[4,5], Erwin Schurr[4, 5] 0000-0002-2640-536X, Pierre Thibault[2, 5] 0000-0001-5993-0331, Michel Desjardins[3, 5] 0000-0002-5684-5980 and Heidi M. McBride[1, 5,*] 0000-0003-4666-2280

[1]Montreal Neurological Institute, McGill University 3801 University Ave, Montreal, Quebec
[2]Institute for Research in Immunology and Cancer (IRIC), Université de Montréal, Montréal, Québec, Canada; Department of Chemistry, Université de Montréal, Montréal, Québec, Canada.
[3]Département de pathologie et biologie cellulaire, Université de Montréal, Montréal, Québec, Canada
[4]Program in Infectious Diseases and Immunity in Global Health, The Research Institute of the McGill University Health Centre; Montreal, QC, Canada and Departments of Human Genetics and Medicine, Faculty of Medicine and Health Science, McGill University, Montreal, Quebec, Canada
[5]ASAP Aligning Science Across Parkinsons

*to whom correspondence be addressed.

Abstract:

A key pathological feature of Parkinson's Disease (PD) is the loss of neuromelanin, an iron chelator within the dopaminergic neurons, which results in iron toxicity thought to result in selective neuronal vulnerability. This implicated iron handling pathways as an early target of research in PD. Given the critical role of PD-related activating mutations in LRRK2 (leucine-rich repeat protein kinase 2) within membrane trafficking pathways we examined the impact of mutant $LRRK2_{G2019S}$ on iron homeostasis within a model macrophage cell line known to have high iron capacity. Proteomics analysis revealed a dysregulation of iron-related proteins in steady state with highly elevated levels of ferritin light chain and a reduction of ferritin heavy chain. LRRK2 mutant cells showed efficient ferritinophagy upon iron chelation, but upon iron overload there was a near complete block in the degradation of the ferritinophagy adaptor NCOA4. Surprisingly, NCOA4 levels were not rescued upon inhibition of the LRRK2 kinase activity in iron overload conditions, nor was the phosphorylation of substrate Rab GTPases. We therefore generated a CRISPR mutation to delete the kinase domain of LRRK2 and express only the Rab-binding armadillo repeat domain. Although the kinase domain was deleted, the truncation mutant of LRRK2 showed strong Rab8 phosphorylation in conditions of iron overload, similar to $LRRK2_{G2019S}$ cells, with the phosphorylated Rab8 accumulating at the plasma membrane. These data indicate that the G2019S mutation acts as a kinase independent, dominant-interfering mutant specifically in conditions of iron overload. Together, our data implicate LRRK2 as a key regulator of iron homeostasis and point to the need for an increased focus on the mechanisms of iron dysregulation in PD.

Introduction:

Age-related neurodegenerative diseases are an increasing burden on the global population. Detailing the precise mechanisms responsible pathology in these complex diseases has been challenging. Hallmark features of Parkinson's Disease (PD) are motor symptoms, namely tremor and rigidity, and selective death of neuromelanin-containing dopamine neurons in the *substantia nigra pars compacta* (SNpc) and *locus coeruleus*. About 5-15% of PD is familial and currently estimates recognize over 50 causal variants and 100 risk alleles (Lim et al., 2024). These highlight contributions of mitochondria and lysosomal function, the spreading of prion-like synuclein filaments, innate and adaptive immune pathways, and more (Cannon and Gruenheid, 2022; Johnson et al., 2019; Tansey et al., 2022). In the remaining ~90% of sporadic PD, it is unclear what the underlying causes may be, although environmental factors like heavy metals or pesticides (Aravindan et al., 2024), and various types of infection (Cannon and Gruenheid, 2022) are under intense investigation.

An early candidate cause of selective vulnerability of dopamine neurons in PD was their high dependence on iron metabolism required for synthesis of dopamine, and production of neuromelanin, which captures and stores excess iron (Jenner, 1989; Sulzer et al., 2000). PD patients show dramatic losses of pigmented neuromelanin, which is a hallmark feature in autopsied brain. The loss of neuromelanin results in higher levels of free iron, which is currently being explored as a biomarker in early-stage PD patients, by high-resolution MRI quantitative susceptibility mapping (Guan et al., 2024). The mechanisms by which iron may be mishandled in the SNpc are understudied, and causality to PD pathology is not clearly established. However, there is increasing speculation that in PD increased iron toxicity may cause ferroptotic cell death, making iron the Achilles' heel of dopaminergic neurons (Jenner, 1989; Masaldan et al., 2019; Riederer et al., 2023). To test these ideas clinically, a series of trials were initiated employing iron chelators in PD patients, with mixed results (Devos et al., 2025). New formulations and approaches are still under investigation, highlighting the importance of a better understanding of the impact of iron on PD pathology.

A common risk factor for inherited PD are variants in the *LRRK2* gene which encodes a large kinase with a complex array of domains including armadillo repeat, ankyrin, WD40, ROC-COR (Ras of complex proteins [ROC] and C-terminal of ROC [COR]) GTPase domains, leucine-rich repeat, and a kinase domain (Alessi and Pfeffer, 2024). The penetrance of PD in carriers of LRRK2 pathogenic variants is typically ~50% at age 70, rising to 75% at 80 years, implicating additional genetic and / or environmental factors in disease progression (Mata et al., 2023). LRRK2 variants have been the subject of intense research efforts which have demonstrated an involvement in cellular functions that span from subcellular protein trafficking (Singh and Muqit, 2020), lysosomal repair/function (Bentley-DeSousa et al., 2025), cytoskeletal dynamics (Leschziner and Reck-Peterson, 2021), ciliogenesis and centrosome cohesion (Jaimon et al., 2025; Li et al., 2024; Lin et al., 2025; Madero-Perez et al., 2018), mitochondrial function (Buck and Sanders, 2025), synaptic transmission (Kuhlmann & Milnerwood 2020), and immune responses (Peter and Strober, 2023). Despite much progress, the molecular basis of LRRK2 pathogenicity remains unclear.

All pathogenic LRRK2 variants, within and outside of LRRK2's kinase domain, increase its serine-threonine kinase activity, including the most common pathogenic substitution p.G2019S ($LRRK2_{G2019S}$) (Mata et al., 2023). In addition to autophosphorylation, LRRK2 substrates include numerous Rab GTPases that regulate vesicular transport; these are hyperphosphorylated in peripheral and central cells from LRRK2 PD patients and models (Alessi

and Pfeffer, 2024; Steger et al., 2016). The downstream impact of each phosphorylated Rab on membrane transport and signaling pathways appears highly dependent on the cell type and context, and the field has not reached consensus on which of the many implicated LRRK2 variant phenotypes are the driver of disease. However, Rab hyperphosphorylation is observed in other genetic forms of PD (e,g., VPS35 (Kadgien et al., 2021; Mir et al., 2018), and idiopathic PD brains (Di Maio et al., 2018). Thus, there is a breadth of evidence associating LRRK2 kinase *gain-of-function* with PD pathogenesis.

In the context of iron handling, previous work reported context-specific changes in iron homeostasis in cells carrying the $LRRK2_{G2019S}$ mutation in HEK293T cells and iPSC-derived microglia (Mamais et al., 2021). It was shown that the phosphorylation of Rab8, a key LRRK2 substrate, reduced its interaction with its GTP exchange factor Rabin8, which in turn led to the lysosomal degradation of the transferrin receptor. Mamais et al (2021) also observed the accumulation of ferritin and free iron in microglia of $LRRK2_{G2019S}$ mice following injections with LPS, although the mechanisms underlying these changes *in vivo* were not established. While iron phenotypes have not been observed consistently within $LRRK2_{G2019S}$ mutant cells, a series of single-cell RNA sequencing experiments did report a cell-specific loss in ferritin heavy chain mRNA within $LRRK2_{G2019S}$ mice, specifically in astrocytes, microglia, and oligodendrocytes (Khan et al., 2024).

Given evidence supporting a contributing role of dysregulated iron homeostasis in PD, we explored the impact of LRRK2 mutations on iron transport and handling. We report the impact of LRRK2 variants and fragments on iron homeostasis in a cultured macrophage model. The data provide evidence that $LRRK2_{G2019S}$ exerts a dominant interfering effect on the response to iron overload, which is resistant to LRRK2 kinase inhibition. Iron overload conditions are not common in healthy physiology but are a significant factor in PD brains. Should this aspect of LRRK2 mutant function be relevant to the death of dopaminergic neurons, our results question the kinase *gain-of-function* mechanism of LRRK2 pathogenicity and argue for caution in the use of kinase inhibitors as a therapeutic approach in patients.

Results:

$LRRK2_{G2019S}$ RAW macrophages have altered iron homeostasis

Macrophages ingest aged red blood cells and have a unique capacity to handle high levels of iron (Winn et al., 2020). Therefore, we considered macrophages, given the high levels of LRRK2 expression (Gardet et al., 2010), as a good model system to interrogate the impact of pathogenic LRRK2 mutations on iron handling. To this end we generated a CRISPR-knock-in RAW264.7 macrophage cell line carrying the $LRRK2_{G2019S}$ mutation. To confirm the increased in LRRK2 kinase activity in this line we probed cell extracts with two phospho-specific antibodies (**Fig. 1A**). LRRK2 autophosphorylation was increased, as seen with an antibody recognizing $LRRK2_{pS1292}$. A second antibody recognizing phosphorylated $Rab8_{T72}$ (with some lower specificity for p-Rab10 and p-Rab35) (Lis et al., 2018), further confirmed an increased kinase activity in the CRISPR-edited $LRRK2_{G2019S}$ macrophages (**Fig1A**). Both phosphorylation events were reversed upon treatment with the LRRK2 kinase inhibitor MLi2 (**Fig. 1A**). These data confirm the successful generation of the *gain-of-function* variant. We then performed unbiased whole cell proteomics and found significant changes in many proteins important for iron homeostasis (**Fig. 1B,C)**. Protein quantification by western blot validated downregulation of the transferrin receptor (TfR) responsible for iron uptake, downregulation of the ferritin heavy chain (FTH), and upregulation of ferritin light chain (FTL), both critical for iron storage (**Fig.**

135 **1D, quantified in Supp Fig. 1A**). Iron is found inside the cell in its reactive ferrous (Fe^{2+}) or
136 mineralized ferric (Fe^{3+}) state. Fe^{2+} is the form required by the cell to forge iron sulfur clusters
137 and heme groups, while excess free ferrous iron can catalyze the generation of free radical
138 species through the Fenton reaction (Galy et al., 2024). This makes Fe^{2+} essential, yet potentially
139 toxic, for the cell. Excess Fe^{2+} is rapidly captured by cytosolic ferritin where iron is harmlessly
140 stored in the mineralized ferric Fe^{3+} state (Chasteen and Harrison, 1999; Melman and Bou-
141 Abdallah, 2020). FTH and FTL together form "cage-like" complexes that can hold up to ~4500
142 atoms of Fe^{3+}. FTH has enzymatic ferroxidase activity required to oxidize Fe^{2+} into Fe^{3+} for safe
143 storage (Melman and Bou-Abdallah, 2020), thus the near total lack of FTH expression in
144 $LRRK2_{G2019S}$ cells should dramatically affect cellular iron storage. We quantified the iron
145 content and composition and found that $LRRK2_{G2019S}$ macrophages have reduced total iron
146 content, marked by a selective loss of mineralized iron Fe^{3+}, and large 2-fold increase in Fe^{2+}
147 content, compared to WT control (**Fig. 1 E).** This result was validated using the fluorescent
148 FerroOrange probe, which reported a similar 2-fold increase of labile Fe^{2+} in $LRRK2_{G2019S}$
149 macrophages (Niwa et al., 2014) (**Supp Fig. 1B,C**).
150 The iron quantification revealed a cellular reduction in total iron, yet we observed excess
151 FTL and reduced TfR which canonically suggests a translational response to iron overload
152 through the iron-response elements (IRE) within their mRNA(Galy et al., 2024; Rouault, 2006).
153 We therefore tested a series of additional iron-related proteins regulated by either the iron-sulfur
154 cluster binding iron responsive protein 1 (IRP1), or the Fe2+ regulated iron response protein 2
155 (IRP2). $LRRK2_{G2019S}$ expression did not elicit any changes in the levels of HERC2/FBXL5/IRP2
156 axis (**Supp Fig. 1D**), indicating IRP2 is not activated. In addition, we found the levels of other
157 proteins harboring IREs such as DMT1 or ferroportin were unaffected in $LRRK2_{G2019S}$
158 macrophages (**Supp Fig. 1D**), implying the IRP1/2 axis is not involved in the upregulation of
159 FTL or downregulation of TfR. This indicates that the changes in FTL and FTH levels are not
160 through canonical iron response element mechanisms.
161 We further tested the enzymatic activity of the iron-sulfur containing IRP1 (also called
162 Aconitase 1 or ACO1) which is often used as a proxy to monitor any deficits in iron-sulfur
163 cluster assemblies (Beinert and Kennedy, 1993). As expected, given the evidence that the
164 translational regulation by IRP1 was unaltered, $LRRK2_{G2019S}$ macrophages did not show any
165 change in ACO1 activity **(Supp Fig. 1E**). This further indicates that the delivery of ferrous Fe^{2+}
166 iron to mitochondria for the biogenesis of iron-sulfur complexes remained intact. Therefore,
167 $LRRK2_{G2019S}$ leads to a significant reduction in total cellular iron (**Fig. 1E**), primarily due to the
168 loss of stored ferric Fe^{3+}, and an increase in ferrous Fe^{2+}, without an impairment of functional
169 delivery of $Fe^{2+}$to mitochondria or the modulation of iron related protein synthesis pathways
170 (**Supp Figs. 1D,E**).
171 FTH is critical for the lysosomal degradation of ferritin complexes through an autophagic
172 process termed ferritinophagy (Dowdle et al., 2014; Kuno et al., 2022; Mancias et al., 2015;
173 Mancias et al., 2014; Ohshima et al., 2022; Zhao et al., 2024). Given the absence of FTH
174 expression, we considered this could cause a block in complex turnover, resulting in the
175 observed increases in FTL levels. To monitor the turnover of FTL we generated WT and
176 $LRRK2_{G2019S}$ macrophages stably expressing N-terminal cherry tagged FTL to visualize its
177 cellular distribution (Ohshima et al., 2022). In untreated WT cells the cherry-FTL signal is
178 primarily distributed within lysotracker green positive lysosomes, with some cytosolic signal
179 (**Fig 1F, quantified in G**). In contrast, $LRRK2_{G2019S}$ macrophages show a highly diffuse cherry-
180 FTL signal in the cytosol and faint lysosomal localization (**Fig 1F third row,G**). This

181 observation is consistent with impaired or inefficient lysosomal targeting of FTL in steady state
182 conditions.
183 To determine whether LRRK2$_{G2019S}$ macrophages were capable of induced ferritin
184 degradation, we induced ferritinophagy with the iron chelator desferoxamine (DFO) to remove
185 iron from the cytoplasm (**Fig. 1F-H**). Ferritinophagy is regulated by the action of nuclear
186 receptor coactivator 4 (NCOA4), the adaptor protein that binds ferritin heavy chain and delivers
187 ferritin cages into the autophagosome (Dowdle et al., 2014; Kuno et al., 2022; Mancias et al.,
188 2014; Ohshima et al., 2022; Zhao et al., 2024)**.** NCOA4 is an iron and iron sulfur cluster binding
189 protein (Kuno et al., 2022; Zhao et al., 2024), and iron levels modulate NCOA4-ferritin
190 interactions allowing the fine tuning of ferritin turnover through formation of liquid-liquid phase
191 separated condensates (LLPS) (Ohshima et al., 2022). Looking first at FTL, DFO treatment
192 increased in the appearance of FTL in lysosomes in WT and LRRK2$_{G2019S}$ macrophages,
193 consistent with functional ferritinophagy (**Fig. 1F second and fourth rows,G**). By western blot
194 we confirmed that iron chelation led to the clearance of FTL in WT and LRRK2$_{G2019S}$
195 macrophages (**Fig. 1H**). With longer exposure the degradative products of FTL were visible in
196 DFO treated LRRK2$_{G2019S}$ macrophages (**Fig. 1H** black arrow). The ferritinophagy adaptor
197 NCOA4 was also highly elevated in LRRK2 mutant cells at steady state (**Fig. 1H**), and we
198 observed that iron chelation led to successful clearance of NCOA4 in LRRK2$_{G2019S}$
199 macrophages, consistent with successful ferritinophagy.
200 The inverse of iron chelation is the response to iron overload, which requires NCOA4 to
201 segregate away from ferritin cages, resulting in a diffuse cytosolic distribution of ferritin that
202 stably mineralizes and stores excess iron as Fe^{3+} (Galy et al., 2024). In high iron conditions
203 NCOA4 binds iron sulfur clusters, which promotes binding of the ubiquitin E3 ligase HERC2 to
204 drive NCOA4 degradation through the proteasome (Zhao et al., 2024). In a second degradation
205 pathway, ferric Fe3+ bound NCOA4 can drive assembly into phase-condensed foci that become
206 internalized into lysosomes through a microautophagy pathway (Kuno et al., 2022). At later time
207 points of iron overload NCOA4 can also carry low levels of ferritin into the lysosomes through
208 microautophagy to maintain pools of labile iron (Kuno et al., 2022). The precise regulation of
209 these distinct mechanisms remains under intense investigation. In our experiments with ferrous
210 ammonium sulfate (FAS) to induce iron overload, we observe the expected diffuse cytosolic
211 staining of FTL in WT cells (**Supp Fig. 2A,B**). In LRRK2$_{G2019S}$ macrophages, FTL is already
212 diffuse in untreated cells, which remains the case upon iron overload, with the addition of a few
213 bright foci resembling phase-condensed foci (**Supp Fig. 2A,B**).
214 A critical distinction emerged between the genotypes when imaging cherry-NCOA4. In
215 WT untreated cells cherry-NCOA4 is seen primarily within lysosomes (**Fig. 2A**), but in
216 LRRK2$_{G2019S}$ macrophages cherry-NCOA4 had limited lysosomal co-localization and appeared
217 in bright cytosolic foci (**Fig. 2A, quantified in 2B,C**). In WT cells treated with FAS NCOA4
218 appeared in bright cytosolic foci and within lysosomes, which became enlarged. In contrast,
219 LRRK2$_{G2019S}$ macrophages showed NCOA4 accumulating in larger bright cytosolic (non-
220 lysosomal) foci, suggesting very little internalization into lysosomes in high iron. Quantification
221 of foci size showed that LRRK2$_{G2019S}$ macrophages had fewer NCOA4 foci with a significant
222 increase in their size relative to WT cells (**Fig. 2B,C**). These quantifications revealed that upon
223 FAS / iron-loading, the number of NCOA4 structures increased ~2-fold in WT cells, whereas the
224 area NCOA4 condensates increased >10 fold in LRRK2$_{G2019S}$ macrophages, relative to WT.
225 Time-lapse imaging of NCOA4 foci revealed their entry into enlarged lysosomes in FAS
226 treated WT cells, as previously described (**Fig. 2D, Supp Video 1**) (Ohshima et al., 2022).

227 Conversely, in LRRK2$_{G2019S}$ cells NCOA4 foci did not associate with lysosomes and were thus
228 seemingly unable to undergo microautophagy (**Fig. 2D, Supp Video 2**). To biochemically
229 confirm bright cytosolic foci reflected the formation of phase-separated condensates, we
230 examined the amount of NCOA4 within Triton-X100 insoluble fractionations (Ohshima et al.,
231 2022). Consistently, total insoluble NCOA4 levels were increased in LRRK2$_{G2019S}$ macrophages
232 (**Fig. 2E**). Addition of bafilomycin to block degradation in lysosomes led to accumulation of
233 NCOA4 in WT cells in both untreated and iron loaded / FAS conditions (**Fig. 2E**). NCOA4 also
234 accumulated in bafilomycin exposed LRRK2$_{G2019S}$ cells, however, in bafilomycin the FAS / iron
235 overload failed to dramatically increase NCOA4 levels further, indicating a block in lysosomal
236 flux (**Fig. 2E**).
237 Live and fixed imaging of lysosomal morphology revealed a significant enlargement of
238 lysosomes in control cells during iron overload, a phenotype that was much reduced in
239 LRRK2$_{G2019S}$ macrophages (**Fig. 2A,D with quantifications in Supp. Fig. 2C-E**). To test the
240 functionality of these lysosomes we employed a proteolytic sensor DQ-BSA red that is
241 internalized into endolysosomes and becomes fluorescent upon cleavage by lysosomal
242 hydrolyases (Marwaha and Sharma, 2017). In steady state there was little difference in lysosomal
243 hydrolytic activity in LRRK2$_{G2019S}$ macrophages, relative to WT (**Fig. 2F**). Upon iron overload
244 we observe a ~50% decrease in activity in control cells, as observed previously (Fernandez et al.,
245 2016). This decrease was exacerbated in LRRK2$_{G2019S}$ macrophages, where lysosomes did not
246 dramatically enlarge (**Supp. Fig. 2C-E**), and showed an ~90% reduction in hydrolytic capacity
247 reported by the probe (**Fig. 2F**). This was not due to a lack of acidification or total lysosomal
248 content, as demonstrated by lysotracker probes that showed increased signal upon iron overload
249 in both genotypes (**Supp Fig. 2F**).
250 To examine the expected LRRK2 kinase-dependency of these phenotypes, we employed
251 the LRRK2 inhibitor MLi-2 (Fell et al., 2015). We applied the drug to untreated and iron
252 overloaded LRRK2$_{G2019S}$ macrophages after FAS treatment. As expected, we observed a clear
253 indication of autophosphorylation activity of LRRK2 (at S1292), along with Rab
254 phosphorylation (**Fig. 2G,H**). Both of these phosphorylation signals were lost upon MLi-2
255 treatment in steady-state conditions (**Fig. 2G,H**). Additionally, MLi-2 reversed the accumulation
256 of NCOA4 in steady-state conditions, indicating that NCOA4 levels are coupled to LRRK2
257 kinase activity (**Fig. 2G,H**). However, upon iron overload the increased levels of NCOA4 and
258 phosphorylated Rab8 were resistant to LRRK2 kinase inhibition, while LRRK2
259 autophosphorylation was efficiently lost, demonstrating target engagement (**Fig. 2G,H**).
260 Moreover, MLi2 treatment did not rescue the alterations in ferritin proteins in untreated cells, nor
261 did it rescue the lysosomal morphology linked to iron overload (**Supp Fig. 2G, H**). This finding
262 indicates that the block in NCOA4 degradation induced by iron overload within LRRK2$_{G2019S}$
263 cells is LRRK2-kinase-independent.
264

265 ### LRRK$_{G2019S}$ impact on iron metabolism is LRRK2-kinase-independent.

266 To understand how the LRRK2 kinase *gain-of-function* mutation could result in kinase-
267 independent phenotypes related to iron handling, we compared a full LRRK2 knockout (LRRK2^{-}
268 $^{/-}$ RAW macrophage line; **LKO**), with a CRISPR edited macrophage line expressing a truncated
269 LRRK2 that retains the N-terminal armadillo repeats, but with the kinase and ROC/COR
270 domains absent (herein; ARM. **Fig 3A**). We suspected that the armadillo domain may play a
271 critical role in the kinase-independent action of the LRRK2$_{G2019S}$ mutant during iron overload.
272 This is because the armadillo domain is responsible for the initial recruitment of LRRK2 to

273 membranes, which could potentially induce an autosomal-dominant function in the context of
274 iron. The armadillo domain binds the GTP-loaded form of either Rab29, Rab32 or Rab38 to
275 drive LRRK2 recruitment, depending on the cell type and context (McGrath et al., 2021;
276 Unapanta et al., 2023). The domain has two additional Rab-binding sites, where the second site
277 was shown to bind Rabs 8 and 10 for phosphorylation, and the third binds Rab12 (Alessi and
278 Pfeffer, 2024; Dhekne et al., 2023). In this way the armadillo domain allows a feed-forward
279 amplification of Rab phosphorylation upon LRRK2 membrane recruitment and activation.
280 We first examined the levels of ferritins and NCOA4 in LKO macrophages, which
281 showed no alteration in these protein levels, indicating that the $LRRK2_{G2019S}$ iron-related
282 phenotypes are not a loss-of-function (**Fig. 3B**). However, $LRRK2_{ARM}$ macrophages showed a
283 pronounced accumulation of NCOA4 and FTL, relative to WT (**Fig. 3B**). To ensure the results
284 were on target, we used CRISPR to introduce a frame-shift at exon 1 of LRRK2 in $LRRK2_{ARM}$
285 cells to generate a second null mutant; this fully rescued the increased NCOA4 and FTL / FTH
286 changes (**Fig. 3D**). The data demonstrate that $LRRK2_{G2019S}$ and $LRRK2_{ARM}$ expression both alter
287 iron homeostasis in a similar manner. Furthermore, this is distinct from *loss-of-function*, is kinase
288 independent, and conveyed by the ARM-containing N-terminus.
289 Similarly to the pattern observed in $LRRK2_{G2019S}$ macrophages (**Fig. 2)**, $LRRK2_{ARM}$ cells
290 exhibited larger and fewer cherry-NCOA4 and cherry-FTL extra-lysosomal aggregates, both in
291 basal and FAS / iron overload conditions (**Fig. 3C-E, Supp Fig. 3A,B**). The extra-lysosomal
292 FTL and NCOA4 formations in $LRRK2_{ARM}$ cells were much larger than those observed in
293 $LRRK2_{G2019S}$ macrophages and lack the spherical shape characteristic of phase-separated
294 compartments (Ohshima et al., 2022). Biochemical analysis of detergent-insolubility confirmed
295 NCOA4 primarily within the detergent-insoluble fraction, which greatly exceeded that of
296 $LRRK2_{G2019S}$ macrophages (**Fig. 3F, long exposure**). Given the biochemical evidence that
297 $LRRK2_{ARM}$ cells exhibited increased detergent-insoluble NCOA4 and FTL (**Fig. 3C**), the
298 immunofluorescence observations likely reflect formation of NCOA4 and FTL aggregates.
299 Additionally, flux experiments using bafilomycin in steady state conditions revealed an acute
300 inability of $LRRK2_{ARM}$ macrophages to target NCOA4 or FTL to lysosomes for degradation
301 (**Fig. 3G**). Moreover, FAS / iron overload impaired the redistribution of cherry-FTL into its
302 cytoplasmic state in $LRRK2_{ARM}$ cells (**Supp Fig. 3A,B**), a phenotype distinct from $LRRK2_{G2019S}$
303 macrophages. Therefore, the turnover of NCOA4 and ferritin is effectively blocked in these cells
304 at steady state. Interestingly, while $LRRK2_{G2019S}$ cells did not exhibit the normal lysosomal
305 enlargement upon iron loading, $LRRK2_{ARM}$ cells demonstrated increased size and roundness of
306 lysosomes upon iron loading, similar to WT cells (**Supp. Fig. 3C-E**).
307 Our evidence that both kinase hyperactive and kinase dead truncated LRRK2 exert
308 significant changes to iron handling led us to examine the impact of both on LRRK2 Rab
309 substrates during iron overload. We observed Rab8 hyper-phosphorylation in $LRRK2_{G2019S}$ cells
310 (**Fig. 1A, 2G**). Consistent with the lack of kinase domain in $LRRK2_{ARM}$ cells, we did not observe
311 increased Rab phosphorylation at steady state (**Fig. 4A**), however we unexpectedly observed
312 hyperphosphorylation of Rab8 in conditions of iron overload at 8 and 24 hours, similar to what is
313 seen in $LRRK2_{G2019S}$ cells. Given the unexpected resistance to MLi-2 in $LRRK2_{G2019S}$ cells upon
314 iron overload / FAS conditions (**Fig. 2G**), and the clear increase in Rab phosphorylation in
315 $LRRK2_{ARM}$ macrophages (**Fig. 4A**), we explored the cellular localization of phosphorylated Rab
316 signal in these conditions. We first validated the phospho-specific Rab8 antibody for
317 immunofluorescence in cells treated with LLOME, where it has been established that LRRK2-
318 mediated Rab8 phosphorylation leads to Rab8 recruitment to damaged lysosomes (**Supp Fig.**

319 **4A**) (Herbst et al., 2020; Mamais et al., 2021). We also observed signal consistent with the
320 previously described recruitment of pRab8 to the centrioles in mitotic cells (Madero-Perez et al.,
321 2018) (**Supp Fig. 4B**). In all genotypes pRab8 was barely detected at steady state (**Fig. 4C**). Iron
322 overload / FAS did not change this pattern in WT or $LRRK2_{ARM\text{-}KO}$ cells; however, in both
323 $LRRK2_{G2019S}$ and $LRRK2_{ARM}$ cells FAS induced a pronounced upregulation and accumulation of
324 pRab8 signal on plasma membrane ruffles and induced blebbing (**Fig. 4B,C**). A similar
325 recruitment of Rab8 to plasma membrane ruffles was previously observed upon activation of
326 Toll-like receptors (Luo et al., 2018; Tong et al., 2021; Wall et al., 2017). There, it was
327 established that TLR-activation of Rab8 recruits its effector PI3Kγ, to generate a signaling
328 platform required to activate AKT/mTOR. We therefore examined AKT phosphorylation at S473
329 as a functional readout of pRab8 recruitment to the cell surface over a time course of FAS
330 treatment. We observed AKT phosphorylation in WT cells, upon FAS / iron overload at 8 hours
331 which was much more pronounced in $LRRK2_{G2019S}$, and $LRRK2_{ARM}$ macrophages (**Fig. 4D**).
332 While this supports the idea that plasma membrane associated pRab8 is activating established
333 Rab8 function, the impact of AKT phosphorylation in these conditions is unclear. Activated
334 AKT is a well characterized driver of cell growth and proliferation; however, our examination of
335 cell growth curves showed a selective block of proliferation in both $LRRK2_{G2019S}$ and
336 $LRRK2_{ARM}$ cells during iron overload (**Fig. 4E**). AKT has also been shown to be protective
337 against ferroptosis through the induction of redox protective pathways, including the
338 phosphorylation and nuclear translocation of NRF2 (Su et al., 2024; Wang et al., 2025).
339 Consistent with this, we found a significant increase in NRF2 nuclear translocation in all cells
340 upon iron overload, which was increased in $LRRK2_{G2019S}$, and even more so in $LRRK2_{ARM}$,
341 macrophages (**Fig. 4F,G)**. Taken together these data provide new evidence for unexpected roles
342 of LRRK mutations on iron handling and the behavior of p-Rab substrates that are resistant to
343 LRRK2 kinase inhibition.
344

345 ## DISCUSSION

346 The literature describing pathogenic LRRK2 mutations in PD overwhelmingly supports a
347 model where a host of different mutations across the protein all result in a gain-of-function
348 kinase activity that has focused clinical trials on LRRK2 kinase inhibitors. Previous studies have
349 identified iron mishandling in LRRK2 mutant cells, and MRI approaches identify iron
350 accumulation as a biomarker in patient carriers of the mutation (Fernandez et al., 2022; Jia et al.,
351 2023; Khan et al., 2024; Mamais et al., 2021; Martinez et al., 2023; Nazish et al., 2023; Oun et
352 al., 2022). Our work supports previous studies and further highlights dysregulated iron
353 metabolism as a potential pathway of interest in LRRK2-related PD. Importantly, we identify
354 $LRRK2_{G2019S}$-related phenotypes that are resistant to MLi2, something that will be of
355 considerable importance in ongoing therapeutic approaches.
356 We identified a very specific condition of iron overload where the introduction of the
357 $LRRK2_{G2019S}$ mutation appears to be dominant interfering, where phenotypes overlap with a
358 truncation mutant lacking the kinase domain entirely. Complete loss of LRRK2 could then
359 rescue the phenotypes including the return of FTL and FTH levels. The most unexpected finding
360 in our study was the clear induction of Rab phosphorylation in $LRRK2_{ARM}$ cells upon iron
361 overload, even though this cell line lacks the LRRK2 kinase domain. We further observed the
362 recruitment of the phosphorylated Rab signal to the plasma membrane in conditions of iron
363 overload specific to the $LRRK2_{G2019S}$ mutant and the $LRRK2_{ARM}$ cells. This may implicate an
364 additional Rab kinase that is activated within LRRK2 mutant cells upon iron overload.

LRRK2's function has been described as driving a "feed-forward" reaction to promote the assembly of activated, phosphorylated Rab GTPases on specific membranes (Alessi and Pfeffer, 2024). The phosphorylated Rab GTPases have been shown to lose binding affinity to GAPs and GDI, reversibility that is critical to constrain and regulate LRRK2 function. This has been shown through the identification of the phosphatase PPM1H (Berndsen et al., 2019; Yeshaw et al., 2023), which allows the dephosphorylation and renewed access to GAPs and GDI to extract the Rabs from the membrane. We speculate that the sequestration of the Rabs through the armadillo domain interferes with the dynamic capacity to degrade NCOA4 by microautophagy, for example. We cannot exclude that LRRK2 may itself have iron sensing capacity that could impact the status of the mutant proteins upon iron overload. One study identified the NCOA4 ubiquitin ligase HERC2 as a LRRK2 binding protein (Imai et al., 2015), although no follow-up studies have confirmed this. One possibility is that LRRK2 could interfere with HERC2s capacity to degrade NCOA4. Given the unexpected nature of some of these findings it will take significant additional work to resolve the underlying mechanisms and context specific actions of LRRK2 in iron metabolism. Instead, we provide an experimental foundation for further exploration of LRRK2s impact in conditions of iron overload. Given the historical focus on iron toxicity within the substantia nigra pars compacta and locus cerulean of PD patients, this may be an important physiological niche where LRRK2 mutations may play pathological roles. With the ongoing clinical trials focused on LRRK2 kinase inhibitors it will be important to monitor their efficacy with biomarkers linked to iron metabolism, perhaps including quantitative susceptibility mapping MRI (Guan et al., 2024; Martinez et al., 2023).

387

388 ## MATERIALS AND METHODS

389

390 ### *Cell culture and reagents*

391 RAW264.7 cells were cultured in DMEM containing high glucose, GLUTA-PLUS and sodium
392 pyruvate (Wisent 319-027-CL) supplemented with 10% heat inactivated fetal bovine serum
393 (Wisent 098159) and antibiotics (Gibco 15-140-122). Cells were cultured at 37°C and 5% CO2
394 in a humidified incubator and regularly tested for mycoplasma.

395

396 Bafilomycin A1 (B1793), Ammonium iron (II) sulfate hexahydrate (FAS) (09719),
397 Deferroxamine mesylate salt (DFO) (D9533) and LLOME (L7393) were purchased from
398 Millipore-Sigma, MLi-2 was purchased from Abcam (ab254528).

399

400 ### *$LRRK2_{G2019S}$ proteomics analysis*

401 Samples were reconstituted in 50 mM ammonium bicarbonate with 10 mM TCEP [Tris(2-
402 carboxyethyl) phosphine hydrochloride; Thermo Fisher Scientific], and vortexed for 1 h at 37°C.
403 Chloroacetamide (Sigma-Aldrich) was added for alkylation to a final concentration of 55 mM.
404 Samples were vortexed for another hour at 37°C. One microgram of trypsin was added, and
405 digestion was performed for 8 h at 37°C. Samples were dried down and solubilized in 5% ACN-
406 4% formic acid (FA). The samples were loaded on a 1.5 µl pre-column (Optimize Technologies,
407 Oregon City, OR). For each run, 1µg of peptides were separated on an home-made reversed-
408 phase column (150-µm i.d. by 200 mm) with a 116-min gradient from 10 to 30% ACN-0.2% FA
409 and a 600-nl/min flow rate on a Easy nLC-1200 connected to a Exploris 480 (Thermo Fisher
410 Scientific, San Jose, CA) with the FAIMS interface. Each proteome was analyzed with 4
411 separate LC-MS/MS runs acquired with a different set of compensation voltages (CV) and a
412 different m/z range: run1 was performed with the CV set-44V-54V-64V-74V from m/z 350 to
413 453, run 2 was performed with the CV set -40V-48V-56V-64V-72V-80V from m/z 451 to 542,
414 run 3 was performed with the CV set -40V-48V-56V-64V-72V-80V from m/z 540 to 661, run 4
415 was performed with the CV set -35V-46V-57V from m/z 659 to 890. Each full MS spectrum
416 acquired at a resolution of 120,000 was followed by tandem-MS (MS-MS) spectra acquisition on
417 the most abundant multiply charged precursor ions for 3s. Tandem-MS experiments were
418 performed using higher energy collision dissociation (HCD) at a collision energy of 34% with an
419 AGC of 50% a resolution of 15,000 and a injection time of 28ms. The data were processed using
420 PEAKS X Pro (Bioinformatics Solutions, Waterloo, ON) and a Uniprot mouse database (16977
421 entries) with trypsin as digestion mode. Mass tolerances on precursor and fragment ions were 10
422 ppm and 0.01 Da, respectively. Fixed modification was carbamidomethyl (C). Variable selected
423 posttranslational modifications were acetylation (N-ter), oxidation (M), deamidation (NQ),
424 phosphorylation (STY).

425

426 ### *Cell lysates, PAGE and immunoblotting*

427 Cells were collected by scraping, washed twice with cold PBS buffer and resuspended in X1
428 PBS containing protease inhibitors (Roche 04693132001) and phosphatase inhibitors (Roche
429 04906837001). Total protein content was quantified by Bradford assay (Bio-Rad 5000006) equal
430 quantities of samples were lysed in Laemmli buffer (10% (vol/vol) glycerol, 2% (wt/vol) SDS,
431 0.005% (wt/vol) bromophenol blue, 60 mMTris-HCl pH 6.8 and 10% (vol/vol) b-
432 mercaptoethanol), and heated 5 minutes at 95 °C prior loading into an SDS-PAGE. Proteins were

433 size separated and transferred to nitrocellulose membranes (Bio-Rad 1620097), blocked for one
434 hour in blocking solution (PBS-tween 0.5% (vol/vol) (PBS-T) containing 5% (w/v) skim milk).
435 After blocking, the membranes were incubated overnight (ON) with primary antibody solution
436 (1:1000 dilution of the antibodies in PBS-T unless otherwise specified). Rabbit anti- FTL
437 (Proteintech 10727-1-AP), FTH (Cell Signaling 4393, clone D1D4), LRRK2 (Abcam,
438 ab133474), GAPDH (Santa Cruz, sc-25778), IRP2 (Proteintech, 29976-1-AP), p-LRRK2 s1292
439 (Abcam, ab203181), NCOA4 (ARA70) (Bethyl, A302-271A), TOMM40 (Proteintech, 18409-1-
440 AP), ferroportin (Alomone labs, AIT-001), p-RAB8A (1:250) (phospho T72) (Abcam,
441 ab230260), RAB8A (1:250) (Cell Signaling, cs-6975), AKT (Cell Signaling, cs-9272), pAKT
442 S473 (Cell Signaling, cs-4060), or mouse anti- TfR (Invitrogen 136800), HERC2 (BD
443 Bioscience, 612366), FBXL5 (Santa Cruz, sc-390102), DMT1 (SLC-11A2) (Santa Cruz, sc-
444 166884), beta-actin (Santa Cruz, sc-8432), PCNA (ZYMED, 13-3900), vinculin (Sigma, V4505)
445 were used in this study. After primary antibody incubation, membranes were washed five times
446 for 10 minutes in PBS-T and incubated for one hour with HRP conjugated secondary antibodies,
447 Donkey anti-mouse (Cytiva, NA931) and donkey anti-rabbit (Cytiva, NA934) in blocking
448 solution (1:5000). Finally, membranes were washed and developed using INTAS ChemoCam
449 (INTAS Science Imaging GmbH) using Western-Lightning PLUS-ECL (Perkin-Elmer).
450

451 *Iron quantification*

452 Fe^{2+}, Fe^{3+} and total iron content was quantified using colorimetric Iron assay kit from Abcam
453 (ab83366) according to manufacturer instructions. Briefly, 2.5 x10^6 cells were seeded in 6 well
454 plate and treated with 100 µM FAS for 16 hrs. Each sample was lysed in 120 µl of assay buffer,
455 ad 50 µl were separated into two wells for quantification of Fe^{2+} and Fe^{3+} content. The rest of the
456 sample was kept for protein concentration estimation. Iron content was obtained by measuring
457 the Abs593 nm and the values were interpolated into the standard curve and then normalized to
458 protein concentration.
459

460 *Aconitase activity assay*

461 Aconitase activity was quantified using Abcam's colorimetric Aconitase activity assay kit
462 (ab83459), according to manufacturer's instructions. Briefly, 2.5 x10^6 cells were harvested,
463 washed with PBS and resuspended in Assay Buffer. Insoluble materials were cleared by
464 centrifuging samples at 800g, the resulting fraction was further centrifuged at 20.000 g for 15
465 minutes and the supernatant was utilized to quantify cytoplasmic aconitase activity. Aconitase
466 activity was measured colorimetrical by measuring absorbance 450 nm, and the enzymatic
467 activity calculated based on the standard curve and normalized to protein concentration.
468

469 *Generation of CRIPSR KI/KO and stable cell lines*

470 *$LRRK2_{G2019S}$ and $LRRK2_{ARM}$ cell lines*

471 The gRNAs for the generation of $LRRK2_{ARM}$ were synthesized using GeneArt precision
472 gRNA synthesis kits (Thermo Fisher) according to the manufacturer's instructions. The gRNA
473 for generation of $LRRK2_{G2019S}$ was designed using TrueDesign Genome editor and
474 synthesized by Thermo Fisher (sequence U*U*G*CGAAGAUUGCGGACUAC + modified
475 scaffold). The $LRRK2_{ARM}$ HDR template used was
476 5'TTCTGTCTAGCCAAAGAGAAGAAATTCAAGTTTTGTG
477 TCCACTTCTTCTTTTTTGTGAAACTAGGTATGTGAGAAAGAGAGCAGTCTTAAA
478 TTGGTGGAACTGTTGCTTAATGGTGGTTGTCGCGAACAAGATGTACGGAAGGCC

479 CTGACCGTAAGCATCCAAAAGGGCGACAGCCAGGTCATCAGCT-3', and the
480 LRRK2$_{G2019S}$ HDR template used was 5'- G*T*A*AACTTGTTCTCCTACCTGGGGTGC
481 CCTCTGATGTCTTTATTCCCATCCTGCAGCAGTACTGTGCGATCGAGTAGTCCGC
482 AATCTTCGCAATGATGGCAGCATTGGGATACAGGGTAAAAAGCAGCACATTGT
483 GGGGCTTCAGGTCACGGTAAATAATCATGGCTGAGTGG*A*G*A-3'. Raw cells
484 were scraped, washed with PBS and electroporated with Cas9 protein and donor HDR
485 templates using Neon transfection system (Thermo Fisher) according to the manufacturer's
486 instructions. After electroporation, cells were plated and cultured for 4 days. Afterwards
487 single cells were seeded in 96 wells and genomic DNA was isolated from single clones. The
488 gRNA target region was amplified by PCR using AmpliTaq Gold 360 master mix (Thermo
489 Fisher). PCR amplicons were sequenced using standard Sanger sequencing.
490
491 *Crispr KO of* LRRK2$_{ARM}$ *(LRRK2$_{ARM-KO}$)*
492 To disrupt the LRRK2 loci in LRRK2$_{ARM}$ macrophages, gRNAs were designed using the
493 webtool CHOP CHOP (https://chopchop.cbu.uib.no), and exons 1 and 7 of mouse *LRRK2* gene
494 were targeted. sgRNA exon1 GTGTTCACCTACTCGGACCGCGG and sgRNA exon 7
495 TGTCCGGTGCTACAATCTTGTGG were purchased from Synthego. Transfection was
496 performed according to manufacturer's instructions. Briefly, ribonucleoparticles (RNPs) were
497 assembled by incubating gRNAs with Cas9 enzyme, followed by reverse transfection using
498 lipofectamine RNAi max transfection reagent (Invitrogen, 13778150) diluted in Optimem (Gibco
499 31985070). Approximately 75,000 cells were seeded in a 24 well together RNPs-transfection
500 solution. 24 hours post transfection, single cells were seeded in 96 wells and several colonies
501 were monitored for the expression of FTH, one clone (D) was isolated with a two base pair
502 deletion ed in exon1 and the maternal mutation in exon 19 detected by Sanger sequencing.
503
504 *Stable cell lines*
505 The stable cells lines expressing mCherry-FTL and mCherry-NCOA4 were generated using
506 retroviral transduction system and stably integrated into the genome. Using Gateway system
507 (Thermo Fisher), cDNAs of FTL (subcloned from Addgene #100153), NCOA4 (DNASU
508 HsCD00043681), were cloned into a pBABE-puro-mCHerrry-GTW, which was engineered by
509 cloning mCherry2 (Addgene # 54563) into pBABEpuro-gateway (Addgene # 51070). For the
510 generation of the retroviral particles, HEK293 phoenix cells were transfected with the different
511 constructs using jetPrime transfection reagent (Polyplus 101000027). Media of the cells was
512 collected 48 hours post-transfection, 0.45 µm filtered and transduced into the macrophages. After
513 24 hours of viral transduction, media was changed and cells selected with 10 µg/ml puromycin
514 until the appearance of resistant colonies. Stable cell lines were used as polyclones.
515 Macrophage cells stably expressing TMEM192-HA (Addgene # 102930) were generated using
516 lentivirus. Lentiviral particles were generated in HEK293T cells using the Lenti-X packaging
517 (Takara 631275) according to manufacturer instructions, after 36 hours media was collected,
518 0.45 µm filtered and added to the RAW macrophages. 24 hours post-transduction cells were
519 selected in 10 µg /ml puromycin until the appearance of resistant colonies. TMEM192-HA
520 expression was confirmed by western blot, and polyclonal cell lines were used in this study.
521
522 *Immunofluorescence and live imaging conditions*
523 Cells were seeded in 13 mm sterile glass coverslips (Thermo Scientific 174950), fixed with 6%
524 PFA for 20 min at 37 °C, washed three times with PBS, and permeabilized with 0.1% Triton X-
525 100 in PBS for 20 minutes. After permeabilization, cells were blocked for 30 min at room

526 temperature in PBS 5% BSA and probed overnight 4 °C with primary antibodies. Rabbit anti
527 LAMP1 (Abcam ab208943), anti p-RAB8 (Abcam, ab230260), mouse anti HA (Sigma H9658)
528 and rat anti LAMP1 (DSHB ab528127) were used in this study. For pRAB8 staining, after PFA
529 fixation, cells were permeabilized with ice cold methanol for 20 minutes at -20^{0}C before
530 blocking. After washing primary antibodies, cells were incubated with the appropriate secondary
531 antibodies (1:3000), donkey anti rabbit coupled to Alexa 488 (Invitrogen, A11006), coupled to
532 Alexa 647 (Invitrogen, 21244), donkey anti rat coupled to Alexa 488 (Invitrogen, A11070),
533 coupled to Alexa 647 (Invitrogen, 21247) or donkey and mouse coupled to Alexa 488
534 (Invitrogen, A11029). After incubation with secondary antibody, slides were washed three
535 additional times with PBS, stained with DAPI (Invitrogen, D1306), washed with double distilled
536 water. Finally, coverslips were mounted on slides using fluorescent mounting media (Dako,
537 S302380-2) prior to imaging.

538 For live imaging approximately 100.000 cells were seeded in glass bottom imaging plates
539 (Cellvis D35C4-20-1.5-N) and stained using normal growing media supplemented with 20 mM
540 HEPES for pH stabilization. For FerroOrange staining cells were incubated for 1 hour in 1 µM
541 FerroOrange (Dojindo F374), in complete media prior to imaging. For labelling late endosomes
542 and lysosomes, cells were incubated in 100 nM LysoTracker Green (Thermo Fisher Scientific,
543 L7526) or LysoTrackerRed (Thermo Fisher Scientific, L7528) for 30 minutes. To label
544 lysosomes to quantify proteolytic activity control or treated cells were incubated for 1 hour with
545 10 µg/mL DQ-BSA red (Thermo Fisher Scientific, D12051) combined with 100 nM
546 LysoTracker Green. Before imaging, HEPES buffer was added to a final concentration of 20
547 mM. For time lapse microscopy, a rate of 1 frame every 2 seconds was acquired. After staining
548 with different dyes and then imaged under controlled temperature and humidity conditions.
549 Immunofluorescence and live imaging experiment were acquired using an Olympus IX83
550 inverted microscope with Yokogawa spinning disk confocal microscope using an UPLANSAPO
551 ×100/1.40 NA oil objective an Andor iXon Ultra EMCCD camera. All the samples were
552 measured under same acquisition and laser intensity conditions.

553 *Quantification of FTL subcellular distribution*
554 Distribution of cherry-FTL was classified into four categories: 1) *diffuse* where most of FTL
555 signal was homogenously distributed across the cellular cytoplasm: 2) *lysosomal*, where the
556 brightest signal inside the cell colocalize with Lamp1 or lysotracker positive structures, 3) *diffuse*
557 *and lysosomal*, where FTL signal is largely diffuse and dim structures positive for Lamp1 or
558 lysotracker could be detected, and 4) *diffuse with condensates*, were FTL distribution was largely
559 diffuse and cytoplasmic but accumulation of bright Lamp1 or lysotracker negative structures
560 were detected. This analysis was not performed blinded.
561

562 *Biochemical fractionation of Triton X-100 soluble and insoluble fractions*
563 To fractionate triton soluble from insoluble fraction biochemically, cells were first resuspended
564 in PBS, protein concentration was estimated, equal amounts of different samples were
565 centrifuged at 600 g for 5 minutes, and cell pellets were resuspended in triton lysis buffer (50
566 mM HEPES pH7.4, 150 mM NaCl, 1%, triton X-100, 1 mM EDTA) supplemented with protease
567 and phosphatase inhibitors (referenced in cell lysate section). Cell lysates were vortexed
568 thoroughly and incubated for 10 minutes on ice followed by centrifugation at 20,000 x g, 4 °C
569 for 20 minutes. Supernatant was transferred to a fresh tube and diluted in Laemmli buffer to

570 generate 1X triton soluble fraction, while the remaining triton insoluble pellet was resuspended
571 in 1X Laemmli sample buffer to the same final volume of the soluble fraction. Samples were
572 then analyzed by SDS-PAGE.
573

574 *Quantification of condensate number and size with image analysis*

575 We used FIJI to quantify the number and area of extra-lysosomal condensates. Images of fixed
576 cells expressing either mCherry-NCOA4, mCherry-FTL or mCherry-FTH and Lamp1 lysosomal
577 marker were acquired using the same laser and exposure conditions and analyzed with the
578 following workflow. This is a cell-based analysis, so first step single cells were selected with a
579 ROI, while the rest of the field was excluded from the analysis. Next, the Lamp1 channel was
580 selected, background subtracted and binarized by automatic thresholding using Otsu method, to
581 obtain a lysosomal mask. Using this lysosomal mask, particle analysis was performed and the
582 ROIs obtained were overlayed with the channel of interest (mCherry- NCOA4, mCherry-FTL or
583 mCherry-FTH), and all the pixels inside this ROIs (lysosomes) were deleted. Finally, the
584 resulting image of the channel of interest was again background subtracted and binarized by
585 automatic thresholding to obtain a mask which was then particle analyzed to quantify the number
586 and size of extra-lysosomal structures.
587

588 *Quantification of FerroOrange integrated fluorescence intensity*

589 FerroOrange fluorescence intensity was quantified in live cells using confocal microscopy and
590 quantified by image analysis using FIJI, several cells per field were selected and their integrated
591 fluorescence intensity was measured. The experiment was repeated 4 times
592

593 *Quantification of lysosomal size and number with image analysis*

594 We used FIJI to analyze and quantified the number and size of lysosomes in single planes. Is
595 important to note that RAW macrophages are not flat cells, thus this number only represents the
596 single plane information and not the total cellular volume. For the analysis lysosomes in
597 $LRRK2_{G2019S}$ macrophages we used cells expressing TMEM192-HA due to its high levels of
598 expression and clear distribution in the lysosomal membrane allowed better edge detection. For
599 $LRRK2_{ARM}$ analysis, LTG was used and the same work flow was followed. Briefly, images were
600 acquired under the same laser power and time exposure conditions and afterwards analyzed with
601 the following workflow. First step, single cells were selected with a ROI while the rest of the
602 field was excluded from the analysis. Next, HA/LTG channel was selected, background
603 subtracted and binarized by automatic Otsu thresholding to obtain a lysosomal mask. Using this
604 lysosomal mask, particle analysis was performed, and the average number and size of lysosomes
605 was recorded per each studied cell.
606

607 *Quantification of lysosomal proteolytic activity by flow cytometry*

608 Cells were seeded and treated with 100 µM FAS for 48 hrs or left untreated for control. To
609 quantify lysosomal proteolytic activity cells were stained with 10 µg/ml of DQ-BSA red and 100
610 nM LysoTracker Green for 1 hour, under the same conditions described in live imaging section.
611 after staining, cells were collected and transferred to a fresh tube in a suspension of 1 $X10^6$ cells/
612 ml.
613 For acquisition single cells suspensions were acquired on an Attune NxT (Thermo Fisher).
614 CS&T performance tracking was done prior to cell acquisition by recommendation of

manufacturer. PMT voltages were determined by Daily CS&T performance tracking. Compensation controls were also acquired. 50 000 events were acquired per sample. Finally, median DQ-BSA red fluorescence and median LysoTracker Green fluorescence from three different repetitions is shown.

Quantification of pRAB8 and NRF2 subcellular distribution

Quantification of pRAB8 and NRF2 distribution was performed qualitatively. Briefly, control or FAS treated cells were stained with endogenous antibodies, and signal from the channel corresponding to the studied protein were equally thresholded among all the cell lines and treatments. The number of cells displaying bright detectable pRAB8 signal at the plasma membrane or NRF2 signal at the nucleus were counted as positive and the total number of cells assessed by DAPI nuclear staining was used to estimate the percentage of positive stained cells. Experiments were repeated at least three times.

Growth curves

To assess growth, on day 0, 150.000 cells were seeded in 12 well plates, and on day 1 cells were either left untreated for control or incubated with 100 µM FAS, quadruplicates measurements were performed in each condition, and cell number was followed for the period of 72 hours.

Statistical analysis

All experiments were performed independently at least three times and quantifications and/or representative images are provided. One-way ANOVA statistical analysis was performed using the GraphPad Prism software (version 8.4.3). Experiments with more than two samples included the multiple comparison analysis. The arithmetic mean with standard deviation of at least three independent experiments are depicted. In addition, the values of all individual cells and the mean of each experiment are shown for the quantifications of size and number of condensates as well as lysosomes. No statistical method was used to predetermine the sample size. The experiments were not randomized; the investigators were not blinded to allocation during experiments and outcome assessment.

ACKNOWLDEGMENTS

We thank Rodolfo Zunino and all members of lab for their help throughout the study. We thank the Desjardins ASAP team and Austen Milnerwood (McGill) for critical comments on the manuscript. We are grateful to Dr. Shawn M Ferguson (Yale) for sharing insightful datasets and discussions during the course of the study.

FUNDING:

Aligning Science Across Parkinson's (MD, HMM)
The study is funded by the joint efforts of Aligning Science Across Parkinson's (ASAP) initiative (to MD, HMM) and the Canadian Institutes of Health Research (to HMM). MJFF administers the grant ASAP-000525 on behalf of ASAP and itself. For the purpose of open access, the author has applied a CC BY public copyright license to all Author Accepted Manuscripts arising from this submission.

Canadian Institutes of Health Research Project Grant (HMM)

AUTHOR CONTRIBUTIONS:

Conceptualization: AG, MD, HMM
Methodology: AG, MN, RZ, JL, AF, YZX, ES, PT, CT, AM
Investigation: AG, MN, JL
Visualization: AG, HMM
Funding acquisition: HMM
Project administration: HMM
Supervision: HMM
Writing – original draft: AG, HMM
Writing – review & editing: AG, MN, MD, HMM

Competing interests: Authors declare that they have no competing interests

Data and materials availability:

The data, code, and key lab materials used and generated in this study are listed in a Key Resource Table alongside their persistent identifiers at [Zenodo DOI – (*to be uploaded after review upon Biorxiv submission*)]. Protocols for this manuscript can be found at protocols.io here (*to be uploaded*): Proteomics datasets are uploaded here: (*to be uploaded*)

680 ## REFERENCES

681

682 Alessi, D.R., and S.R. Pfeffer. 2024. Leucine-Rich Repeat Kinases. *Annu Rev Biochem*. 93:261-
683 287.
684 Aravindan, A., M.E. Newell, and R.U. Halden. 2024. Literature review and meta-analysis of
685 environmental toxins associated with increased risk of Parkinson's disease. *Sci Total*
686 *Environ*. 931:172838.
687 Beinert, H., and M.C. Kennedy. 1993. Aconitase, a two-faced protein: enzyme and iron
688 regulatory factor. *FASEB J*. 7:1442-1449.
689 Bentley-DeSousa, A., D. Clegg, and S.M. Ferguson. 2025. LRRK2, lysosome damage, and
690 Parkinson's disease. *Curr Opin Cell Biol*. 93:102482.
691 Berndsen, K., P. Lis, W.M. Yeshaw, P.S. Wawro, R.S. Nirujogi, M. Wightman, T. Macartney,
692 M. Dorward, A. Knebel, F. Tonelli, S.R. Pfeffer, and D.R. Alessi. 2019. PPM1H
693 phosphatase counteracts LRRK2 signaling by selectively dephosphorylating Rab
694 proteins. *Elife*. 8.
695 Buck, S.A., and L.H. Sanders. 2025. LRRK2-mediated mitochondrial dysfunction in Parkinson's
696 disease. *Biochem J*. 482:721-739.
697 Cannon, T., and S. Gruenheid. 2022. Microbes and Parkinson's disease: from associations to
698 mechanisms. *Trends in microbiology*. 30:749-760.
699 Chasteen, N.D., and P.M. Harrison. 1999. Mineralization in ferritin: an efficient means of iron
700 storage. *J Struct Biol*. 126:182-194.
701 Devos, D., O. Rascol, W.G. Meissner, A. Foubert-Samier, S. Lewis, C. Tranchant, M. Anheim,
702 D. Maltete, P. Remy, K. Eggert, H. Pape, C. Geny, P. Couratier, C. Carroll, R. Sheridan,
703 D. Burn, N. Pavese, J. Raw, D. Berg, O. Suchowersky, L.V. Kalia, A. Evans, S. Drapier,
704 T. Danaila, A. Schnitzler, J.C. Corvol, G. Defer, N.T. Temin, C. Fradette, F. Tricta, C.
705 Moreau, and g. a Parkinson's disease study. 2025. Therapeutic modalities of deferiprone
706 in Parkinson's disease: SKY and EMBARK studies. *J Parkinsons Dis*. 15:72-86.
707 Dhekne, H.S., F. Tonelli, W.M. Yeshaw, C.Y. Chiang, C. Limouse, E. Jaimon, E. Purlyte, D.R.
708 Alessi, and S.R. Pfeffer. 2023. Genome-wide screen reveals Rab12 GTPase as a critical
709 activator of Parkinson's disease-linked LRRK2 kinase. *Elife*. 12.
710 Di Maio, R., E.K. Hoffman, E.M. Rocha, M.T. Keeney, L.H. Sanders, B.R. De Miranda, A.
711 Zharikov, A. Van Laar, A.F. Stepan, T.A. Lanz, J.K. Kofler, E.A. Burton, D.R. Alessi,
712 T.G. Hastings, and J.T. Greenamyre. 2018. LRRK2 activation in idiopathic Parkinson's
713 disease. *Sci Transl Med*. 10.
714 Dowdle, W.E., B. Nyfeler, J. Nagel, R.A. Elling, S. Liu, E. Triantafellow, S. Menon, Z. Wang,
715 A. Honda, G. Pardee, J. Cantwell, C. Luu, I. Cornella-Taracido, E. Harrington, P. Fekkes,
716 H. Lei, Q. Fang, M.E. Digan, D. Burdick, A.F. Powers, S.B. Helliwell, S. D'Aquin, J.
717 Bastien, H. Wang, D. Wiederschain, J. Kuerth, P. Bergman, D. Schwalb, J. Thomas, S.
718 Ugwonali, F. Harbinski, J. Tallarico, C.J. Wilson, V.E. Myer, J.A. Porter, D.E. Bussiere,
719 P.M. Finan, M.A. Labow, X. Mao, L.G. Hamann, B.D. Manning, R.A. Valdez, T.
720 Nicholson, M. Schirle, M.S. Knapp, E.P. Keaney, and L.O. Murphy. 2014. Selective
721 VPS34 inhibitor blocks autophagy and uncovers a role for NCOA4 in ferritin degradation
722 and iron homeostasis in vivo. *Nat Cell Biol*. 16:1069-1079.
723 Fell, M.J., C. Mirescu, K. Basu, B. Cheewatrakoolpong, D.E. DeMong, J.M. Ellis, L.A. Hyde, Y.
724 Lin, C.G. Markgraf, H. Mei, M. Miller, F.M. Poulet, J.D. Scott, M.D. Smith, Z. Yin, X.
725 Zhou, E.M. Parker, M.E. Kennedy, and J.A. Morrow. 2015. MLi-2, a Potent, Selective,

726 and Centrally Active Compound for Exploring the Therapeutic Potential and Safety of
727 LRRK2 Kinase Inhibition. *J Pharmacol Exp Ther*. 355:397-409.
728 Fernandez, B., E. Fdez, P. Gomez-Suaga, F. Gil, I. Molina-Villalba, I. Ferrer, S. Patel, G.C.
729 Churchill, and S. Hilfiker. 2016. Iron overload causes endolysosomal deficits modulated
730 by NAADP-regulated 2-pore channels and RAB7A. *Autophagy*. 12:1487-1506.
731 Fernandez, B., P. Olmedo, F. Gil, E. Fdez, Y. Naaldijk, P. Rivero-Rios, F. Bracher, C. Grimm,
732 G.C. Churchill, and S. Hilfiker. 2022. Iron-induced cytotoxicity mediated by
733 endolysosomal TRPML1 channels is reverted by TFEB. *Cell death & disease*. 13:1047.
734 Galy, B., M. Conrad, and M. Muckenthaler. 2024. Mechanisms controlling cellular and systemic
735 iron homeostasis. *Nat Rev Mol Cell Biol*. 25:133-155.
736 Gardet, A., Y. Benita, C. Li, B.E. Sands, I. Ballester, C. Stevens, J.R. Korzenik, J.D. Rioux, M.J.
737 Daly, R.J. Xavier, and D.K. Podolsky. 2010. LRRK2 is involved in the IFN-gamma
738 response and host response to pathogens. *J Immunol*. 185:5577-5585.
739 Guan, X., M. Lancione, S. Ayton, P. Dusek, C. Langkammer, and M. Zhang. 2024.
740 Neuroimaging of Parkinson's disease by quantitative susceptibility mapping.
741 *Neuroimage*. 289:120547.
742 Herbst, S., P. Campbell, J. Harvey, E.M. Bernard, V. Papayannopoulos, N.W. Wood, H.R.
743 Morris, and M.G. Gutierrez. 2020. LRRK2 activation controls the repair of damaged
744 endomembranes in macrophages. *EMBO J*. 39:e104494.
745 Imai, Y., Y. Kobayashi, T. Inoshita, H. Meng, T. Arano, K. Uemura, T. Asano, K. Yoshimi, C.L.
746 Zhang, G. Matsumoto, T. Ohtsuka, R. Kageyama, H. Kiyonari, G. Shioi, N. Nukina, N.
747 Hattori, and R. Takahashi. 2015. The Parkinson's Disease-Associated Protein Kinase
748 LRRK2 Modulates Notch Signaling through the Endosomal Pathway. *PloS Genet*.
749 11:e1005503.
750 Jaimon, E., Y.E. Lin, F. Tonelli, O. Antico, D.R. Alessi, and S.R. Pfeffer. 2025. Restoration of
751 striatal neuroprotective pathways by kinase inhibitor treatment of Parkinson's disease-
752 linked LRRK2-mutant mice. *Sci Signal*. 18:eads5761.
753 Jenner, P. 1989. Clues to the mechanism underlying dopamine cell death in Parkinson's disease.
754 *J Neurol Neurosurg Psychiatry*. Suppl:22-28.
755 Jia, R., Y. Liu, K. Shuai, C. Zhou, L. Chen, L. Zhu, and X.M. Wu. 2023. The Relationship
756 between Iron and LRRK2 in a 6-OHDA-Induced Parkinson's Disease Model. *Int J Mol*
757 *Sci*. 24.
758 Johnson, M.E., B. Stecher, V. Labrie, L. Brundin, and P. Brundin. 2019. Triggers, Facilitators,
759 and Aggravators: Redefining Parkinson's Disease Pathogenesis. *Trends Neurosci*. 42:4-
760 13.
761 Kadgien, C.A., A. Kamesh, and A.J. Milnerwood. 2021. Endosomal traffic and glutamate
762 synapse activity are increased in VPS35 D620N mutant knock-in mouse neurons, and
763 resistant to LRRK2 kinase inhibition. *Mol Brain*. 14:143.
764 Khan, S.S., E. Jaimon, Y.E. Lin, J. Nikoloff, F. Tonelli, D.R. Alessi, and S.R. Pfeffer. 2024. Loss
765 of primary cilia and dopaminergic neuroprotection in pathogenic LRRK2-driven and
766 idiopathic Parkinson's disease. *Proc Natl Acad Sci U S A*. 121:e2402206121.
767 Kuno, S., H. Fujita, Y.K. Tanaka, Y. Ogra, and K. Iwai. 2022. Iron-induced NCOA4
768 condensation regulates ferritin fate and iron homeostasis. *EMBO Rep*. 23:e54278.
769 Leschziner, A.E., and S.L. Reck-Peterson. 2021. Structural Biology of LRRK2 and its
770 Interaction with Microtubules. *Movement disorders : official journal of the Movement*
771 *Disorder Society*. 36:2494-2504.

772 Li, X., H. Zhu, B.T. Huang, X. Li, H. Kim, H. Tan, Y. Zhang, I. Choi, J. Peng, P. Xu, J. Sun, and
773 Z. Yue. 2024. RAB12-LRRK2 complex suppresses primary ciliogenesis and regulates
774 centrosome homeostasis in astrocytes. *Nat Commun*. 15:8434.
775 Lim, S.Y., A.H. Tan, A. Ahmad-Annuar, N.U. Okubadejo, K. Lohmann, H.R. Morris, T.S. Toh,
776 Y.W. Tay, L.M. Lange, S. Bandres-Ciga, I. Mata, J.N. Foo, E. Sammler, J.C.E. Ooi, A.J.
777 Noyce, N. Bahr, W. Luo, R. Ojha, A.B. Singleton, C. Blauwendraat, and C. Klein. 2024.
778 Uncovering the genetic basis of Parkinson's disease globally: from discoveries to the
779 clinic. *Lancet Neurol*. 23:1267-1280.
780 Lin, Y.E., E. Jaimon, F. Tonelli, and S.R. Pfeffer. 2025. Pathogenic LRRK2 mutations cause loss
781 of primary cilia and Neurturin in striatal parvalbumin interneurons. *Life Sci Alliance*. 8.
782 Lis, P., S. Burel, M. Steger, M. Mann, F. Brown, F. Diez, F. Tonelli, J.L. Holton, P.W. Ho, S.L.
783 Ho, M.Y. Chou, N.K. Polinski, T.N. Martinez, P. Davies, and D.R. Alessi. 2018.
784 Development of phospho-specific Rab protein antibodies to monitor in vivo activity of
785 the LRRK2 Parkinson's disease kinase. *Biochem J*. 475:1-22.
786 Luo, L., A.A. Wall, S.J. Tong, Y. Hung, Z. Xiao, A.A. Tarique, P.D. Sly, E. Fantino, M.P.
787 Marzolo, and J.L. Stow. 2018. TLR Crosstalk Activates LRP1 to Recruit Rab8a and
788 PI3Kgamma for Suppression of Inflammatory Responses. *Cell reports*. 24:3033-3044.
789 Madero-Perez, J., E. Fdez, B. Fernandez, A.J. Lara Ordonez, M. Blanca Ramirez, P. Gomez-
790 Suaga, D. Waschbusch, E. Lobbestael, V. Baekelandt, A.C. Nairn, J. Ruiz-Martinez, A.
791 Aiastui, A. Lopez de Munain, P. Lis, T. Comptdaer, J.M. Taymans, M.C. Chartier-Harlin,
792 A. Beilina, A. Gonnelli, M.R. Cookson, E. Greggio, and S. Hilfiker. 2018. Parkinson
793 disease-associated mutations in LRRK2 cause centrosomal defects via Rab8a
794 phosphorylation. *Mol Neurodegener*. 13:3.
795 Mamais, A., J.H. Kluss, L. Bonet-Ponce, N. Landeck, R.G. Langston, N. Smith, A. Beilina, A.
796 Kaganovich, M.C. Ghosh, L. Pellegrini, R. Kumaran, I. Papazoglou, G.R. Heaton, R.
797 Bandopadhyay, N. Maio, C. Kim, M.J. LaVoie, D.C. Gershlick, and M.R. Cookson.
798 2021. Mutations in LRRK2 linked to Parkinson disease sequester Rab8a to damaged
799 lysosomes and regulate transferrin-mediated iron uptake in microglia. *PloS Biol*.
800 19:e3001480.
801 Mancias, J.D., L. Pontano Vaites, S. Nissim, D.E. Biancur, A.J. Kim, X. Wang, Y. Liu, W.
802 Goessling, A.C. Kimmelman, and J.W. Harper. 2015. Ferritinophagy via NCOA4 is
803 required for erythropoiesis and is regulated by iron dependent HERC2-mediated
804 proteolysis. *Elife*. 4.
805 Mancias, J.D., X. Wang, S.P. Gygi, J.W. Harper, and A.C. Kimmelman. 2014. Quantitative
806 proteomics identifies NCOA4 as the cargo receptor mediating ferritinophagy. *Nature*.
807 509:105-109.
808 Martinez, M., M. Ariz, I. Alvarez, G. Castellanos, M. Aguilar, J. Hernandez-Vara, N. Caballol,
809 A. Garrido, A. Bayes, D. Vilas, M.J. Marti, C. Catalonian Neuroimaging Parkinson's
810 disease, P. Pastor, C.O. de Solorzano, and M.A. Pastor. 2023. Brainstem neuromelanin
811 and iron MRI reveals a precise signature for idiopathic and LRRK2 Parkinson's disease.
812 *NPJ Parkinsons Dis*. 9:62.
813 Marwaha, R., and M. Sharma. 2017. DQ-Red BSA Trafficking Assay in Cultured Cells to Assess
814 Cargo Delivery to Lysosomes. *Bio Protoc*. 7.
815 Masaldan, S., A.I. Bush, D. Devos, A.S. Rolland, and C. Moreau. 2019. Striking while the iron is
816 hot: Iron metabolism and ferroptosis in neurodegeneration. *Free Radic Biol Med*.
817 133:221-233.

818 Mata, I., P. Salles, M. Cornejo-Olivas, P. Saffie, O.A. Ross, X. Reed, and S. Bandres-Ciga. 2023.
819 LRRK2: Genetic mechanisms vs genetic subtypes. *Handb Clin Neurol*. 193:133-154.
820 McGrath, E., D. Waschbusch, B.M. Baker, and A.R. Khan. 2021. LRRK2 binds to the Rab32
821 subfamily in a GTP-dependent manner via its armadillo domain. *Small GTPases*. 12:133-
822 146.
823 Melman, A., and F. Bou-Abdallah. 2020. Iron mineralization and core dissociation in
824 mammalian homopolymeric H-ferritin: Current understanding and future perspectives.
825 *Biochim Biophys Acta Gen Subj*. 1864:129700.
826 Mir, R., F. Tonelli, P. Lis, T. Macartney, N.K. Polinski, T.N. Martinez, M.Y. Chou, A.J.M.
827 Howden, T. Konig, C. Hotzy, I. Milenkovic, T. Brucke, A. Zimprich, E. Sammler, and
828 D.R. Alessi. 2018. The Parkinson's disease VPS35[D620N] mutation enhances LRRK2-
829 mediated Rab protein phosphorylation in mouse and human. *Biochem J*. 475:1861-1883.
830 Nazish, I., A. Mamais, A. Mallach, C. Bettencourt, A. Kaganovich, T. Warner, J. Hardy, P.A.
831 Lewis, J. Pocock, M.R. Cookson, and R. Bandopadhyay. 2023. Differential LRRK2
832 Signalling and Gene Expression in WT-LRRK2 and G2019S-LRRK2 Mouse Microglia
833 Treated with Zymosan and Mli2. *Cells*. 13.
834 Niwa, M., T. Hirayama, K. Okuda, and H. Nagasawa. 2014. A new class of high-contrast Fe(II)
835 selective fluorescent probes based on spirocyclized scaffolds for visualization of
836 intracellular labile iron delivered by transferrin. *Org Biomol Chem*. 12:6590-6597.
837 Ohshima, T., H. Yamamoto, Y. Sakamaki, C. Saito, and N. Mizushima. 2022. NCOA4 drives
838 ferritin phase separation to facilitate macroferritinophagy and microferritinophagy. *J Cell*
839 *Biol*. 221.
840 Oun, A., A. Soliman, M. Trombetta-Lima, A. Tzepapadaki, D. Tsagkari, A. Kortholt, and A.M.
841 Dolga. 2022. LRRK2 protects immune cells against erastin-induced ferroptosis.
842 *Neurobiol Dis*. 175:105917.
843 Peter, I., and W. Strober. 2023. Immunological Features of LRRK2 Function and Its Role in the
844 Gut-Brain Axis Governing Parkinson's Disease. *J Parkinsons Dis*. 13:279-296.
845 Riederer, P., T. Nagatsu, M.B.H. Youdim, M. Wulf, J.M. Dijkstra, and J. Sian-Huelsmann. 2023.
846 Lewy bodies, iron, inflammation and neuromelanin: pathological aspects underlying
847 Parkinson's disease. *J Neural Transm (Vienna)*. 130:627-646.
848 Rouault, T.A. 2006. The role of iron regulatory proteins in mammalian iron homeostasis and
849 disease. *Nature chemical biology*. 2:406-414.
850 Singh, P.K., and M.M.K. Muqit. 2020. Parkinson's: A Disease of Aberrant Vesicle Trafficking.
851 *Annu Rev Cell Dev Biol*. 36:237-264.
852 Steger, M., F. Tonelli, G. Ito, P. Davies, M. Trost, M. Vetter, S. Wachter, E. Lorentzen, G.
853 Duddy, S. Wilson, M.A. Baptista, B.K. Fiske, M.J. Fell, J.A. Morrow, A.D. Reith, D.R.
854 Alessi, and M. Mann. 2016. Phosphoproteomics reveals that Parkinson's disease kinase
855 LRRK2 regulates a subset of Rab GTPases. *Elife*. 5.
856 Su, H., C. Peng, and Y. Liu. 2024. Regulation of ferroptosis by PI3K/Akt signaling pathway: a
857 promising therapeutic axis in cancer. *Front Cell Dev Biol*. 12:1372330.
858 Sulzer, D., J. Bogulavsky, K.E. Larsen, G. Behr, E. Karatekin, M.H. Kleinman, N. Turro, D.
859 Krantz, R.H. Edwards, L.A. Greene, and L. Zecca. 2000. Neuromelanin biosynthesis is
860 driven by excess cytosolic catecholamines not accumulated by synaptic vesicles. *Proc*
861 *Natl Acad Sci U S A*. 97:11869-11874.

862 Tansey, M.G., R.L. Wallings, M.C. Houser, M.K. Herrick, C.E. Keating, and V. Joers. 2022.
863 Inflammation and immune dysfunction in Parkinson disease. *Nature reviews.*
864 *Immunology*. 22:657-673.
865 Tong, S.J., A.A. Wall, Y. Hung, L. Luo, and J.L. Stow. 2021. Guanine nucleotide exchange
866 factors activate Rab8a for Toll-like receptor signalling. *Small GTPases*. 12:27-43.
867 Unapanta, A., F. Shavarebi, J. Porath, Y. Shen, C. Balen, A. Nguyen, J. Tseng, W.S. Leong, M.
868 Liu, P. Lis, S.M. Di Pietro, and A. Hiniker. 2023. Endogenous Rab38 regulates LRRK2's
869 membrane recruitment and substrate Rab phosphorylation in melanocytes. *J Biol Chem*.
870 299:105192.
871 Wall, A.A., L. Luo, Y. Hung, S.J. Tong, N.D. Condon, A. Blumenthal, M.J. Sweet, and J.L.
872 Stow. 2017. Small GTPase Rab8a-recruited Phosphatidylinositol 3-Kinase gamma
873 Regulates Signaling and Cytokine Outputs from Endosomal Toll-like Receptors. *J Biol*
874 *Chem*. 292:4411-4422.
875 Wang, L., W. Yang, and Y. Song. 2025. Impairing Ferroptosis Through the PI3K/Akt/Nrf2
876 Pathway: The Way for Nerve Growth Factor to Mitigate Hypoxia-induced
877 Cardiomyocyte Damage. *Cell Biochem Biophys*. 83:2023-2033.
878 Winn, N.C., K.M. Volk, and A.H. Hasty. 2020. Regulation of tissue iron homeostasis: the
879 macrophage "ferrostat". *JCI Insight*. 5.
880 Yeshaw, W.M., A. Adhikari, C.Y. Chiang, H.S. Dhekne, P.S. Wawro, and S.R. Pfeffer. 2023.
881 Localization of PPM1H phosphatase tunes Parkinson's disease-linked LRRK2 kinase-
882 mediated Rab GTPase phosphorylation and ciliogenesis. *Proc Natl Acad Sci U S A*.
883 120:e2315171120.
884 Zhao, H., Y. Lu, J. Zhang, Z. Sun, C. Cheng, Y. Liu, L. Wu, M. Zhang, W. He, S. Hao, and K.
885 Li. 2024. NCOA4 requires a [3Fe-4S] to sense and maintain the iron homeostasis. *J Biol*
886 *Chem*. 300:105612.
887

FIGURE LEGENDS

Figure 1: LRRK2$_{G2019S}$ RAW macrophages show changes in iron homeostasis

A- Western blot analysis on whole cell lysates of pRAB8$_{T72}$ and pLRRK2$_{S1292}$ in WT and LRRK2$_{G2019S}$ macrophages. PCNA serves as loading control (C). **B**-Volcano plot showing differentially expressed proteins in LRRK2$_{G2019S}$ compared to WT macrophages. On the x axis fold change (FC) and in the y axis -log base 10 of the adjusted statistical significance (p.adj) are plotted. Dashed lines represent the cut-offs for analysis, proteins with a fold change larger than -/+ 1-fold and p.adj greater than 1.3 ($p<0.05$) were considered as differentially expressed. Red dots depict some of the differentially expressed proteins important for iron metabolism. **C** – Heat map and table depicting the fold change and the role of the main iron related proteins differentially expressed in LRRK2$_{G2019S}$ macrophages. FC= fold change. Raw data found in Supplementary Table 1. **D-** Western blot analysis on whole cell lysates of iron markers in WT and LRRK2$_{G2019S}$ macrophages. GAPDH serves as loading control. **E-** Levels of ferric (Fe^{3+}) and ferrous (Fe^{2+}) iron in WT and LRRK2 $_{G2019S}$ macrophages. Iron is quantified as µmoles of iron per mg of protein. Prior to iron quantification, cells were fed overnight with 100 µM ferrous ammonium sulfate (FAS). The means of three separate experiment are shown. **F-** Representative images of cherry-FTL distribution in WT and LRRK2$_{G2019S}$ macrophages control or treated with DFO 250 µM for 24 hours. Lysosomes were stained with LTG. Scale bar 4 µm, inset 1µm.**G-** Qualitative classification of cherry-FTL distribution shown in F. The means of three separate experiment are shown. **H-** Western blot analysis of NCOA4, FTL and FTH and TfR levels on whole cell lysates of WT and LRRK2$_{G2019S}$ macrophages, control or treated for 24 hours with 250 µM DFO. PCNA serves as loading control. Black arrow indicates proteolytic cleavage product of FTL.

Supplementary Figure 1: LRRK2$_{G2019S}$ RAW macrophages show changes in iron homeostasis

A- Densitometry analysis of FTH, FTL and TfR levels in WT and LRRK2$_{G2019S}$ macrophages. Band intensities were normalized to loading controls, the means of three separate experiment are shown. One-way ANOVA statistical analysis and standard deviation (SD) are shown. **B-** Representative images of WT and LRRK2 $_{G2019S}$ macrophages stained with Fe^{2+}sensor FerroOrange. Fluorescence intensity of the images was color coded using FIJIs thermal LUT. Scale bar 5 µm. **C-** Quantification of FerroOrange fluorescence intensity of data shown in B. The means and single values of three separate experiment are shown. One-way ANOVA statistical analysis and standard deviation (SD) are shown.**D-** Western blot analysis on whole cell lysates of IRP2 FBXL5 HERC2, ferroportin (FPT) and DMT1 in WT and LRRK2$_{G2019S}$ macrophages. GAPDH serves as loading control. **E-** Quantification of cytosolic Aconitase activity in WT and LRRK2$_{G2019S}$ RAW macrophages, expressed as activity units per mg of protein. The means of three separate experiment are shown. One-way ANOVA statistical analysis and standard deviation (SD) are shown.

Figure 2: LRRK2$_{G2019S}$ expressing cells cannot clear NCOA4 phase-separated condensates upon iron overload

A- Representative images of cherry-NCOA4 distribution in WT and LRRK2$_{G2019S}$ macrophages control or treated for 16 hours with FAS 100 µM. Lysosomes were stained with anti LAMP1 antibody. Scale bar 4 µm, inset 1µm. **B-** Quantification of the average size of cytoplasmic cherry-NCOA4 condensates calculated as μm^2 per cell of data shown in A. The means and single

934 values of three separate experiment are shown. Multiple comparison one-way ANOVA statistical
935 analysis and standard deviation (SD) are shown. **C**-Quantification of average number of
936 cytoplasmic cherry-NCOA4 condensates per cell of data shown in A. The means and single
937 values of three separate experiment are shown. Multiple comparison one-way ANOVA statistical
938 analysis and standard deviation (SD) are shown. **D**- Representative time-lapse sequences of
939 cherry-NCOA4 condensates in WT and LRRK2$_{G2019S}$ macrophages treated for 48 hours with
940 FAS 100 µM. Lysosomes were stained with LTG. Time-lapse experiments were acquired for
941 5 minutes, capturing both channels every 2 seconds. Scale bar 4 µm, inset 1µm. **E**- Western blot
942 analysis of triton x-100 soluble and triton x-100 insoluble NCOA4 levels in WT and
943 LRRK2$_{G2019S}$ RAW macrophages control or treated with 25 nM bafilomycin for 3 hours. **F**- Flow
944 cytometric measurement of median BSA-DQ red fluorescence intensity in WT and LRRK2$_{G2019S}$
945 macrophages control or treated for 48 hours with FAS 100 µM. The median of three separate
946 experiment is shown. **G**- Western blot analysis of NCOA4 and pRAB8 on whole cell extracts of
947 LRRK2$_{G2019S}$macrophages treated for 16 hours with FAS 100 µM and then treated with 1 µM
948 MLi-2 for 8 hours. Phosphorylation levels of LRRK2 on S1292 is used as positive control,
949 ACTIN serves as loading control. **H**- Densitometry analysis of data shown in G. Band intensities
950 were normalized to loading controls and the means of three separate experiment are shown.
951

952 ## Supplementary Figure 2: LRRK2$_{G2019S}$ expressing cells cannot clear NCOA4 phase-separated
953 condensates upon iron overload

954 **A**- Representative images of cherry-FTL distribution in WT and LRRK2$_{G2019S}$ macrophages
955 control or treated for 16 hours with FAS 100 µM. Lysosomes were stained with LTG. Scale bar
956 4 µm, inset 1µm. **B**- Qualitative classification of cherry-FTL distribution of data shown in A.
957 The means of three separate experiment are shown. **C**- Representative images of lysosomal
958 morphology of WT and LRRK2$_{G2019S}$ macrophages control or treated for 24 or 48 hours with
959 FAS 100 µM. Cells expressing TMEM192-HA in their lysosomal surface were stained with anti
960 HA antibody. Scale bar 4 µm. **D**- Quantification of average number of lysosomes per cell of the
961 experiment shown in C. The means and single values of three separate experiment are shown. **E**-
962 Quantification of the average lysosomal size per cell of data shown in C. The means and single
963 values of three separate experiment are shown. **F**- Flow cytometric measurement of median LTG
964 fluorescence intensity in WT and LRRK2$_{G2019S}$ macrophages control or treated for 48 hours with
965 FAS 100 µM. The median of three separate experiment is shown. **G**- Western blot analysis of
966 FTL and FTH levels on whole cell extracts of WT and LRRK2$_{G2019S}$ macrophages control or
967 treated for 4 or 8 hours with 1 µM MLi-2. Phosphorylation levels of LRRK2 on S1292 were
968 used as positive control, ACTIN serves as loading control. **H**- Representative images of
969 lysosome morphology of WT and LRRK2$_{G2019S}$ macrophages treated for 48 hours with FAS 100
970 µM and then incubated for 8 hours with 1 µM MLi-2 in the presence of iron. Lysosomes were
971 stained with anti LAMP1 antibody. Scale bar 5 µm.
972
973

974 ## Figure 3: LRRK2 truncation lacking kinase domain reveals similar phenotypes to kinase-active
975 mutation

976 **A**- Schematic representation of LRRK2's domain composition. LRRK2$_{ARM}$ clone was generated
977 by directing a gRNAs to exon 19, ARM= armadillo, ANK=ankryn, LRR= leucine rich repeat,
978 ROC+COR = GTPase domain, KIN=kinase domain and WD40 domain. **B**- Western blot
979 analysis on whole cell lysates of NCOA4, FTL, FTH and TfR in WT and LRRK2$_{KO}$, LRRK2$_{ARM}$

980 and LRRK2 $_{ARM\text{-}KO}$ macrophages. PCNA serves as loading control. **C**- Representative images of
981 cherry-NCOA4 distribution in WT and LRRK2$_{ARM}$ macrophages control or treated for 16 hours
982 with FAS 100 µM. Lysosomes were stained with anti LAMP1 antibody. Scale bar 4 µm, inset
983 1µm. **D**- Quantification of the average size of cytoplasmic cherry-NCOA4 condensates
984 calculated as µm^2 per cell of data shown in C. The means and single values of three separate
985 experiment are shown. Multiple comparison one-way ANOVA statistical analysis and standard
986 deviation (SD) are shown **E**- Quantification of average number of cytoplasmic cherry-NCOA4
987 condensates per cell of data shown in C. The means and single values of three separate
988 experiment are shown. One-way ANOVA statistical analysis and standard deviation (SD) are
989 shown. **F**- Western blot analysis of NCOA4, FTL and FTH in triton x-100 soluble and triton x-
990 100 insoluble fractions of WT, LRRK$_{ARM}$ and LRRK2$_{G2019S}$ macrophages. GAPDH and serve as
991 loading control. **G** - Western blot analysis of bafilomycin dependent lysosomal flux of NCOA4,
992 FTL and FTH in WT and LRRK2$_{ARM}$ macrophages. Cells were treated for 2 and 16 hours with
993 25 nM bafilomycin. PCNA serves as loading control.
994

995 Supplementary Figure 3: LRRK2 truncation lacking kinase domain reveals similar phenotypes to
996 kinase-active mutation

997 **A**- Representative images of cherry-FTL distribution in WT and LRRK2 ARM macrophages
998 control or treated for 16 hours with FAS 100 µM. Lysosomes were stained with anti LAMP1
999 antibody. Scale bar 4 µm, inset 1µm. **B**- Quantification of the average size of cytoplasmic
1000 cherry-FTL condensates calculated as µm^2 per cell of data shown in A. The means and single
1001 values of three separate experiment are shown. Multiple comparison one-way ANOVA statistical
1002 analysis and standard deviation (SD) are shown. **C**- Representative images of lysosome
1003 morphology of WT and LRRK2$_{ARM}$ macrophages treated for 48 hours with FAS 100 µM.
1004 Lysosomes were stained with LTG. Scale bar 4 µm. **D**- Quantification of average number of
1005 lysosomes per cell of the experiment shown in C. The means and single values of three separate
1006 experiment are shown. Multiple comparison one-way ANOVA statistical analysis and standard
1007 deviation (SD) are shown. **E**- Quantification of the average lysosomal size per cell of data
1008 shown in C. The means and single values of three separate experiment are shown. Multiple
1009 comparison one-way ANOVA statistical analysis and standard deviation (SD) are shown.
1010

1011 Figure 4: LRRK2 mutations drive dominant, aberrant localization of phosphorylated Rab8 and Akt
1012 activation upon iron overload
1013

1014 **A-** Western blot analysis of p-RAB8 in WT and LRRK2$_{ARM}$ and LRRK2$_{G2019S}$ macrophages
1015 control or treated with FAS 100 µM. VINCULIN serves as loading control **B**- Representative
1016 images of endogenous pRAB8A distribution in WT, LRRK2$_{G2019S}$, LRRK2$_{ARM}$ and LRRK2$_{ARM}$
1017 $_{KO}$ macrophages control of treated for 8 hours with FAS 100 µM. Lysosomes were stained with
1018 anti LAMP1 antibody. Scale bar 10 µm, inset 5 µm. **C**- Quantification of the percentage of cells
1019 showing positive pRAB8 signal at plasma membrane. The means of three separate experiments
1020 are shown. **D**- Western blot analysis of p-AKT S473 in WT, LRRK2$_{G2019S}$ and LRRK2$_{ARM}$
1021 macrophages control or treated with FAS 100 µM. PCNA serves as loading control. **E**- Growth
1022 curve of WT, LRRK2$_{G2019S}$, LRRK$_{ARM}$ and LRRK2 $_{ARM\ KO}$ macrophages. Cell count was
1023 followed for 3 days in the presence or absence of 100 µM FAS. Each point shows the average
1024 and standard deviation of 4 measurement. **F**- Representative images of endogenous NRF2
1025 distribution in WT, LRRK2$_{G2019S}$ and LRRK$_{ARM}$ macrophages for 48 hours with FAS 100 µM.

1026 Cell nuclei were stained with DAPI, lysosomes were stained with anti LAMP1 antibody. Scale
1027 bar 10 µm. **G-** Quantification of the percentage of cells showing nuclear NRF2 translocation.
1028 The means and single values of three separate experiment are shown. One-way ANOVA
1029 statistical analysis and standard deviation (SD) are shown.
1030
1031 Supplementary Figure 4: LRRK2 mutations drive dominant, aberrant localization of
1032 phosphorylated Rab8 and Akt activation upon iron overload
1033
1034 **A**-Representative images of endogenous pRAB8A distribution in WT macrophages control of
1035 treated for 3 hours with LLOME 1 mM. Lysosomes were stained with anti LAMP1 antibody.
1036 Scale bar 5 µm. **B**-Representative images of endogenous pRAB8A distribution in mitotic WT
1037 macrophages. Nuclei are stained with DAPI. Scale bar 5 µm.
1038
1039 Supplementary Table 1:
1040 Proteomics dataset from LRRK2G2019S and wild type RAW macrophages.
1041
1042
1043

FIGURE 1

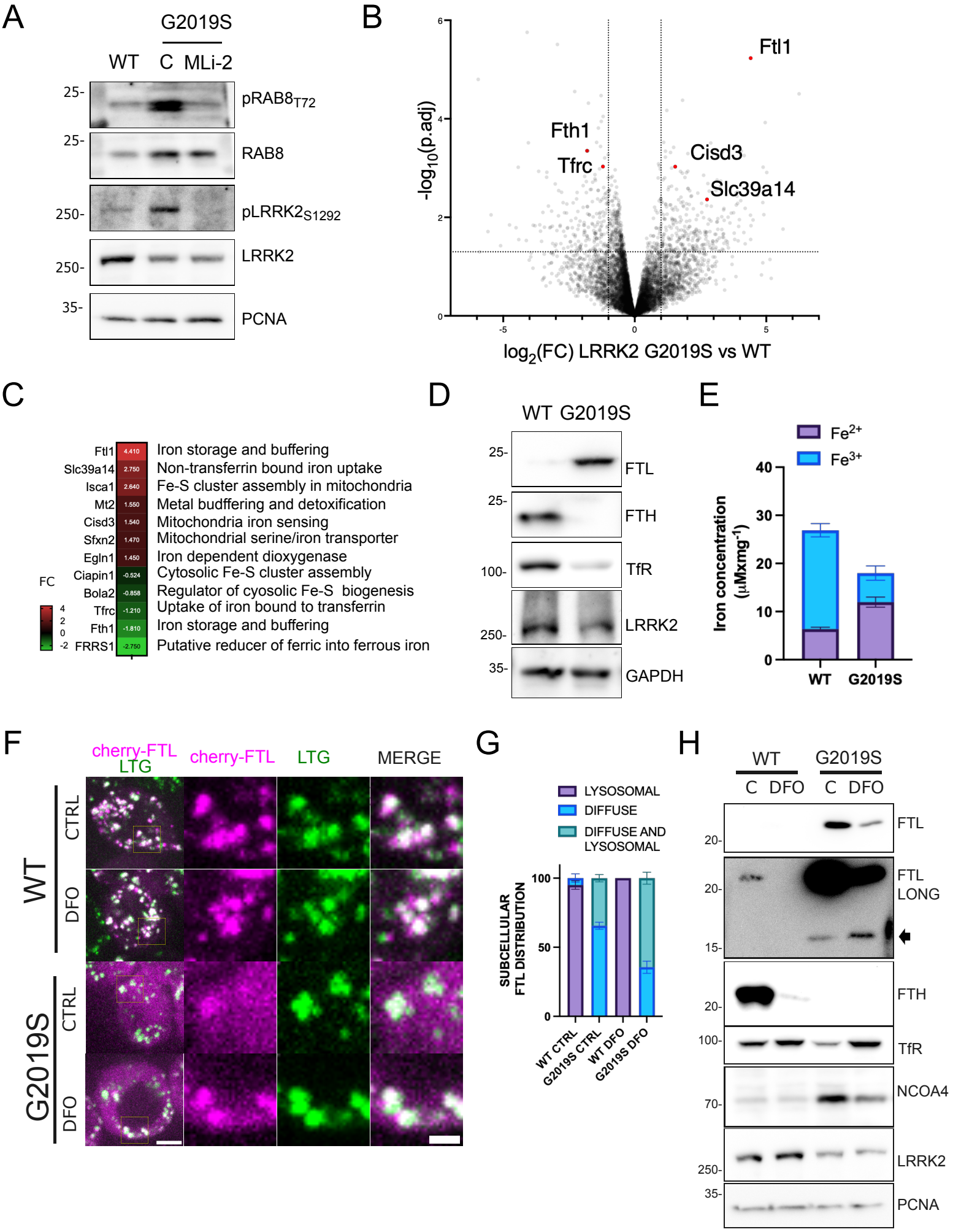
A
G2019S
WT
C
MLi-2
25-
pRAB8T72
25-
RAB8
250-
pLRRK2S1292
250-
LRRK2
35-
PCNA
B
Ftl1
Fth1
Tfrc
Cisd3
Slc39a14
-log10(p.adj)
log2(FC) LRRK2 G2019S vs WT
C
Ftl1 4.410 Iron storage and buffering
Slc39a14 2.750 Non-transferrin bound iron uptake
Isca1 2.640 Fe-S cluster assembly in mitochondria
Mt2 1.550 Metal budffering and detoxification
Cisd3 1.540 Mitochondria iron sensing
Sfxn2 1.470 Mitochondrial serine/iron transporter
Egln1 1.450 Iron dependent dioxygenase
Ciapin1 -0.524 Cytosolic Fe-S cluster assembly
Bola2 -0.858 Regulator of cyosolic Fe-S biogenesis
Tfrc -1.210 Uptake of iron bound to transferrin
Fth1 -1.810 Iron storage and buffering
FRRS1 -2.750 Putative reducer of ferric into ferrous iron
FC
D
WT G2019S
25-
FTL
25-
FTH
100-
TfR
250-
LRRK2
35-
GAPDH
E
Fe2+
Fe3+
Iron concentration (µMxmg-1)
WT
G2019S
F
cherry-FTL LTG
cherry-FTL
LTG
MERGE
WT
CTRL
DFO
G2019S
CTRL
DFO
G
LYSOSOMAL
DIFFUSE
DIFFUSE AND LYSOSOMAL
SUBCELLULAR FTL DISTRIBUTION
WT CTRL
G2019S CTRL
WT DFO
G2019S DFO
H
WT
G2019S
C
DFO
C
DFO
20-
FTL
20-
FTL LONG
15-
20-
FTH
100-
TfR
70-
NCOA4
250-
LRRK2
35-
PCNA

SUPPLEMENTARY FIG1

A

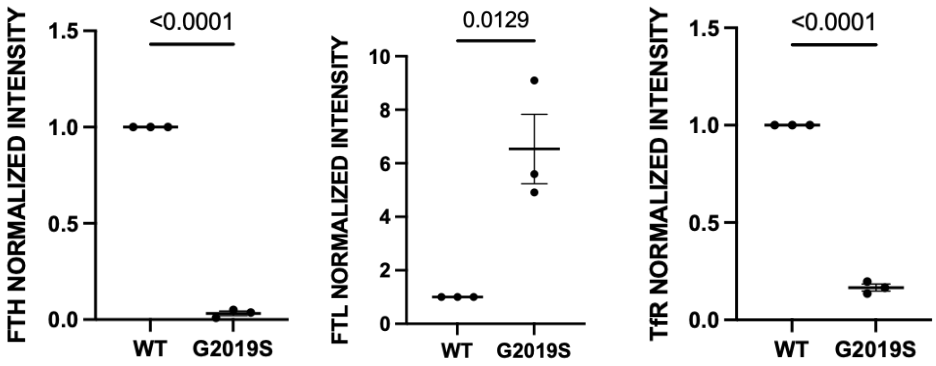

B

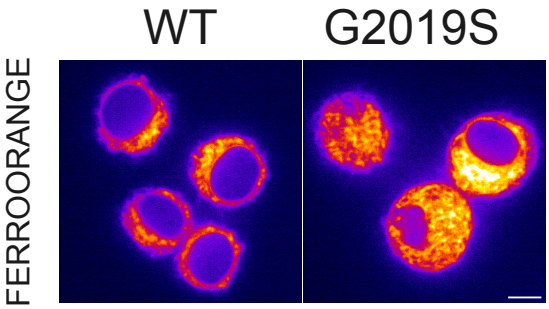

D

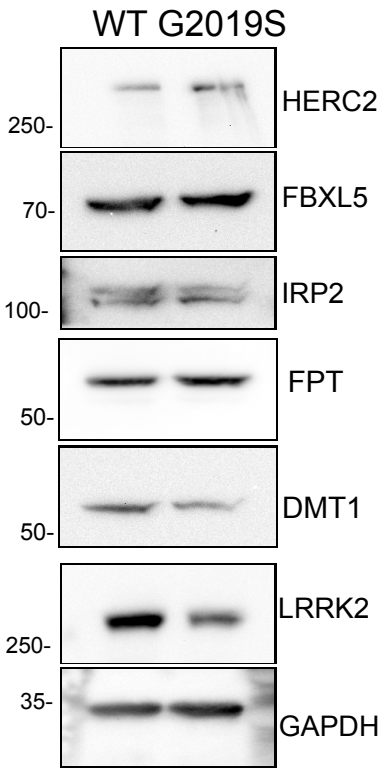

E

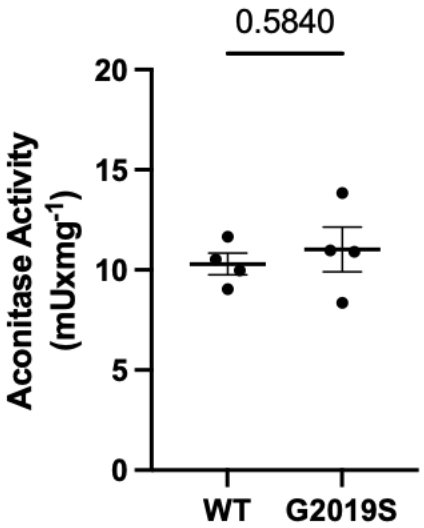

C

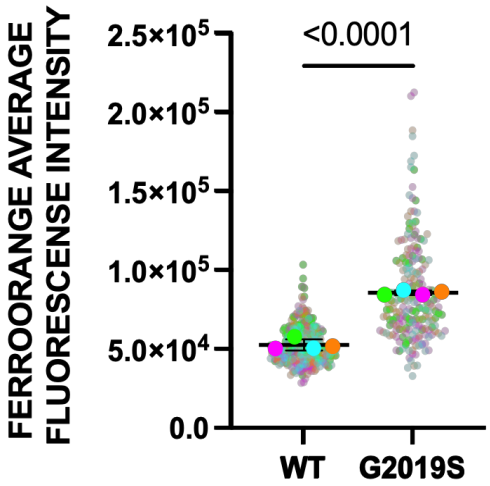

FIGURE2

A

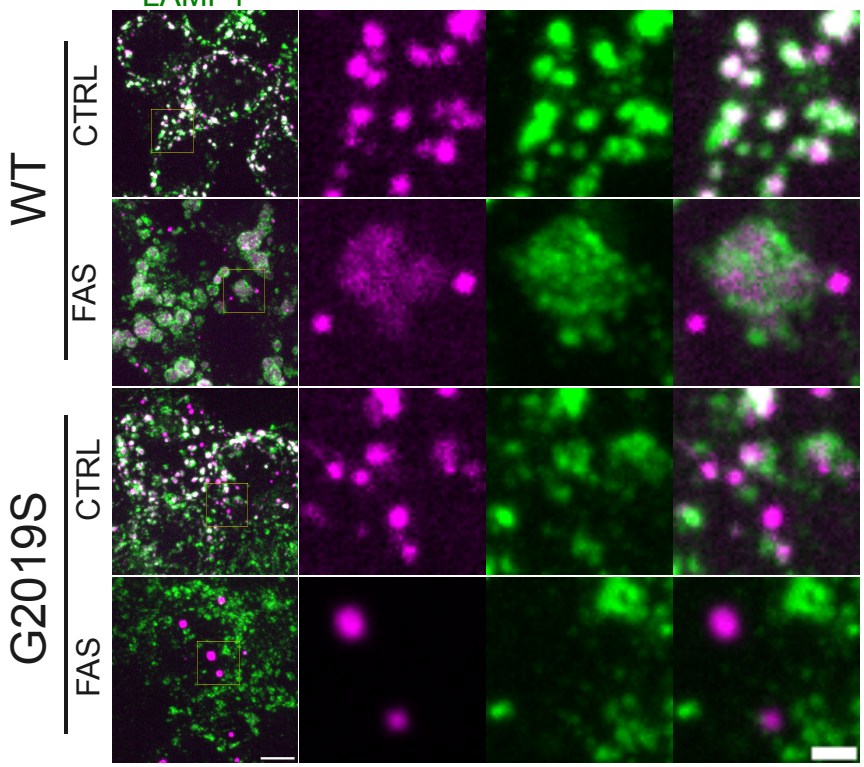

B

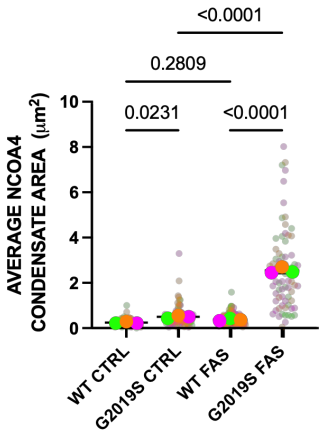

C

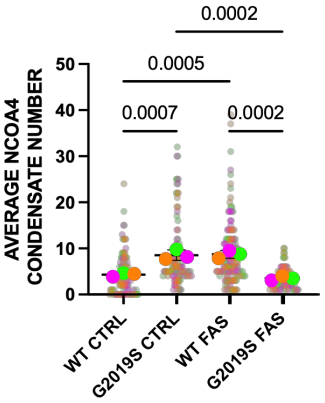

D

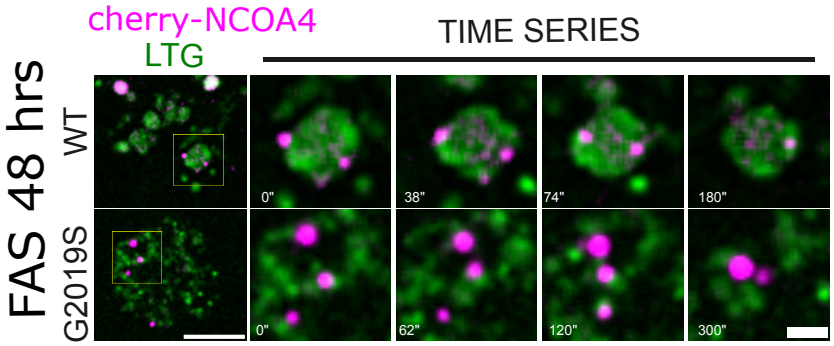

E

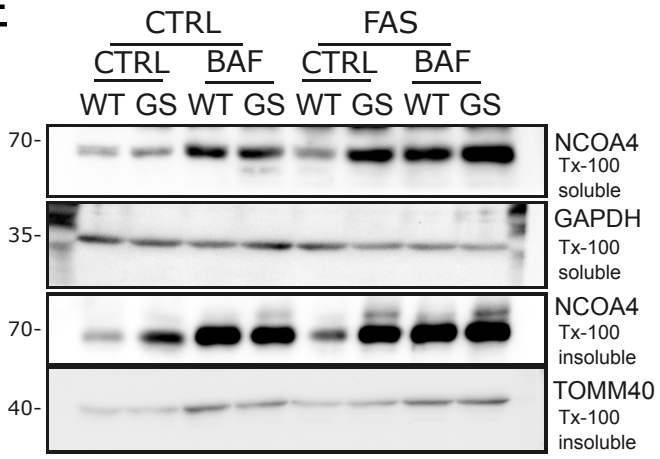

F

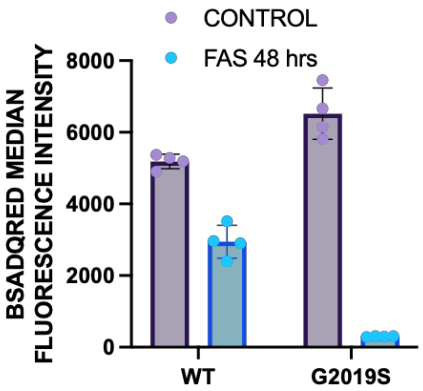

G

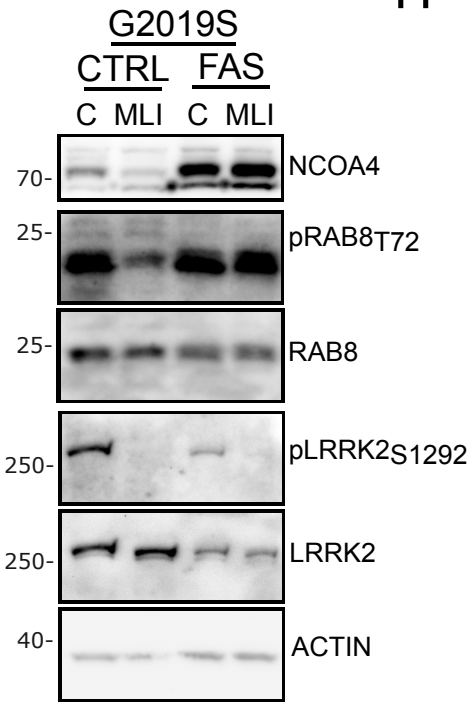

H

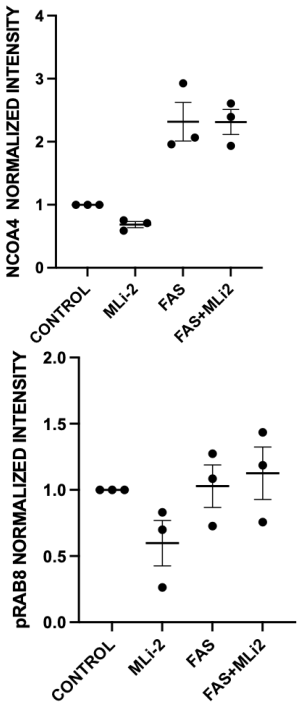

SUPPLEMENTARY FIG 2

A

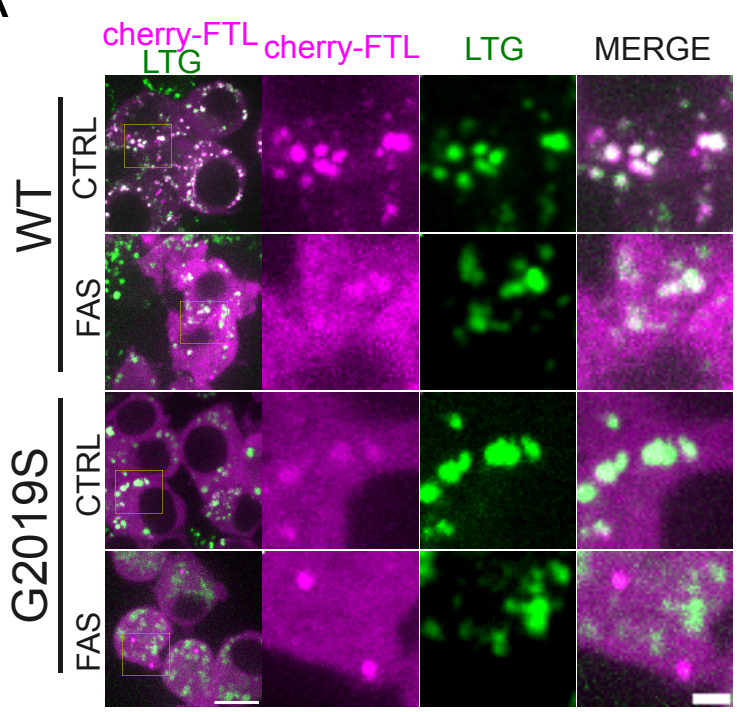

B

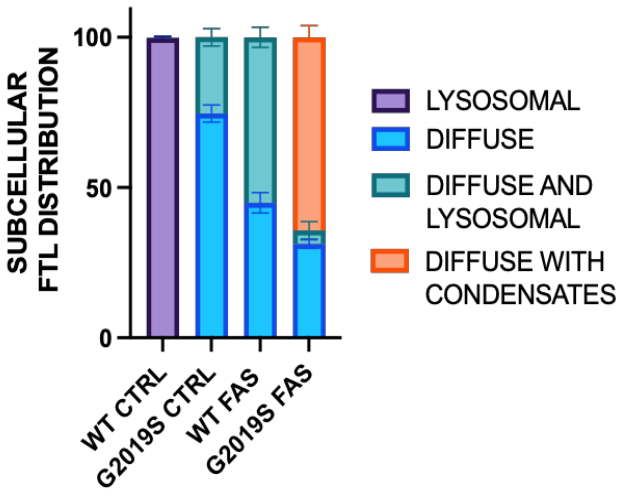

C

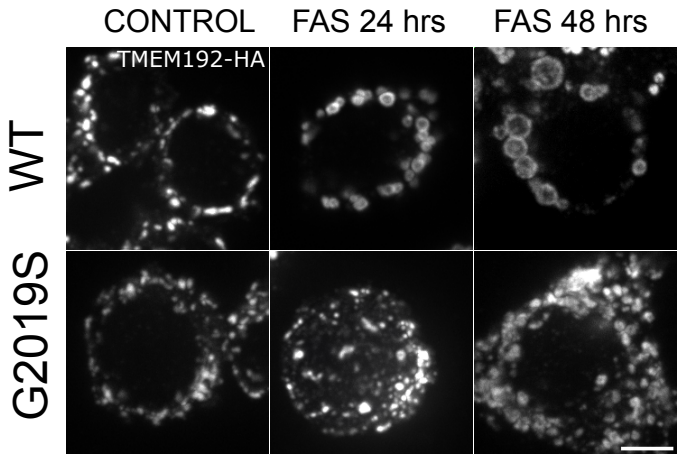

D

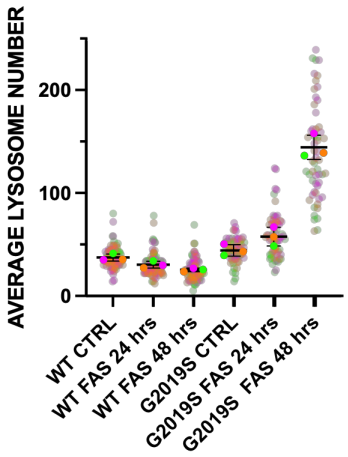

E

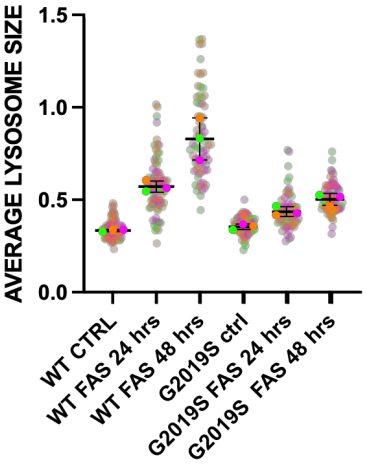

F

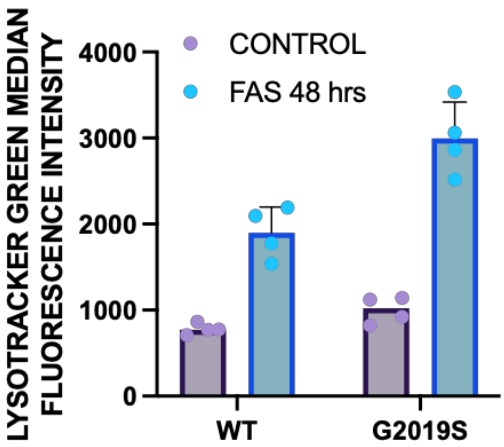

G

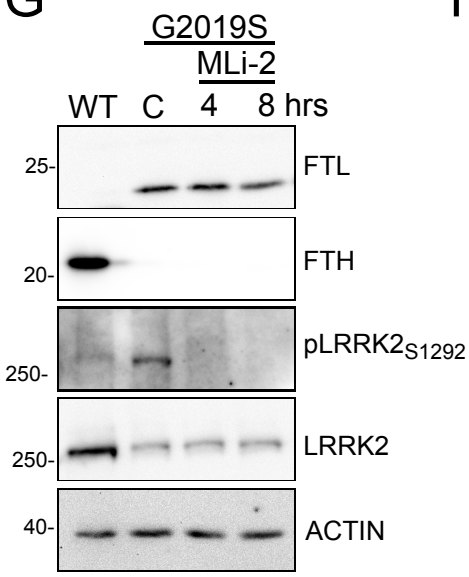

H

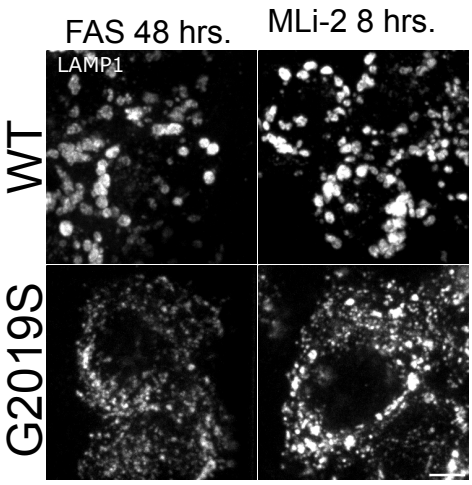

FIGURE 3

A

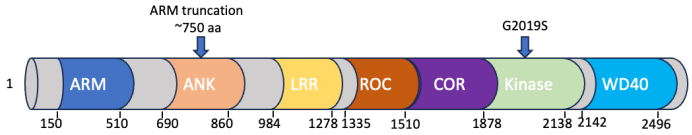

B

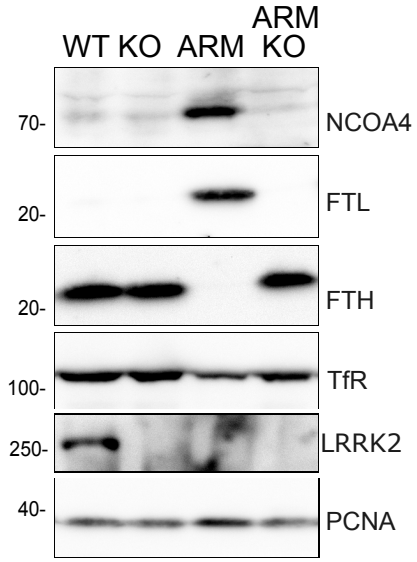

C

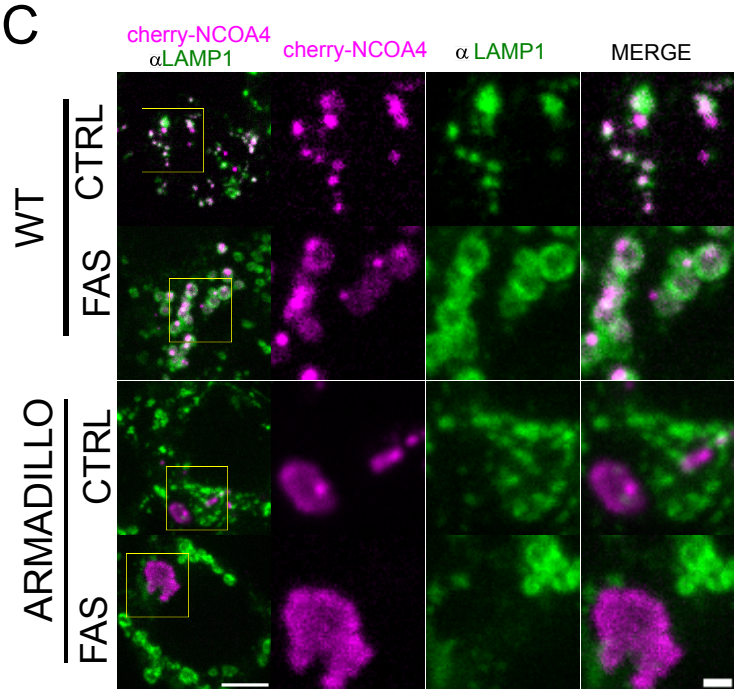

D

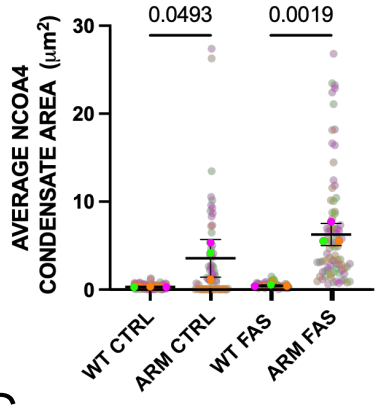

E

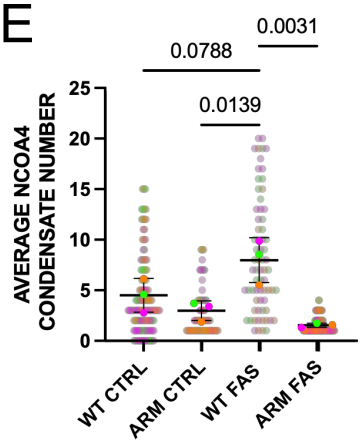

F

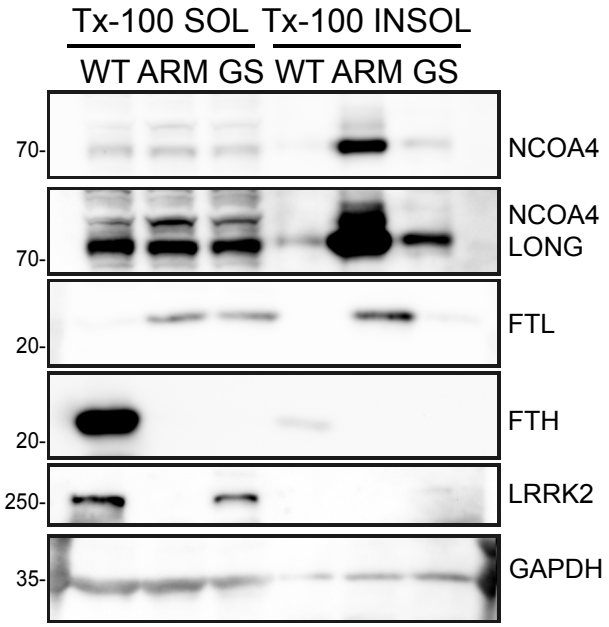

G

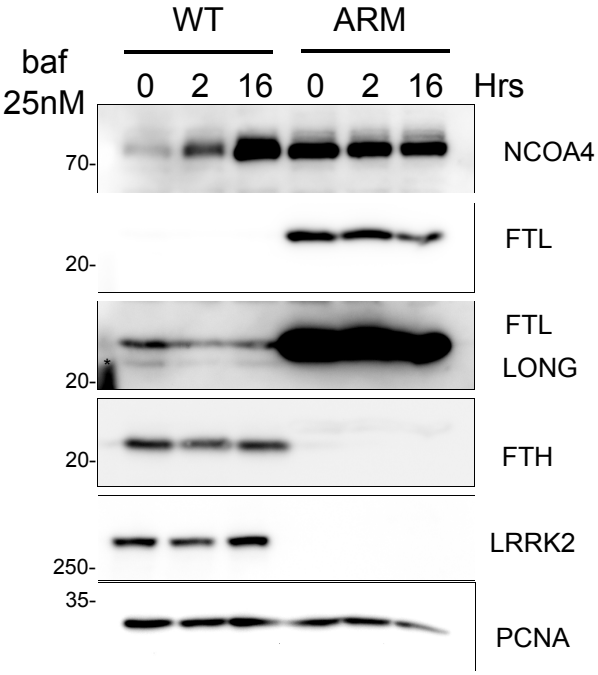

SUPPLEMENTARY FIG 3

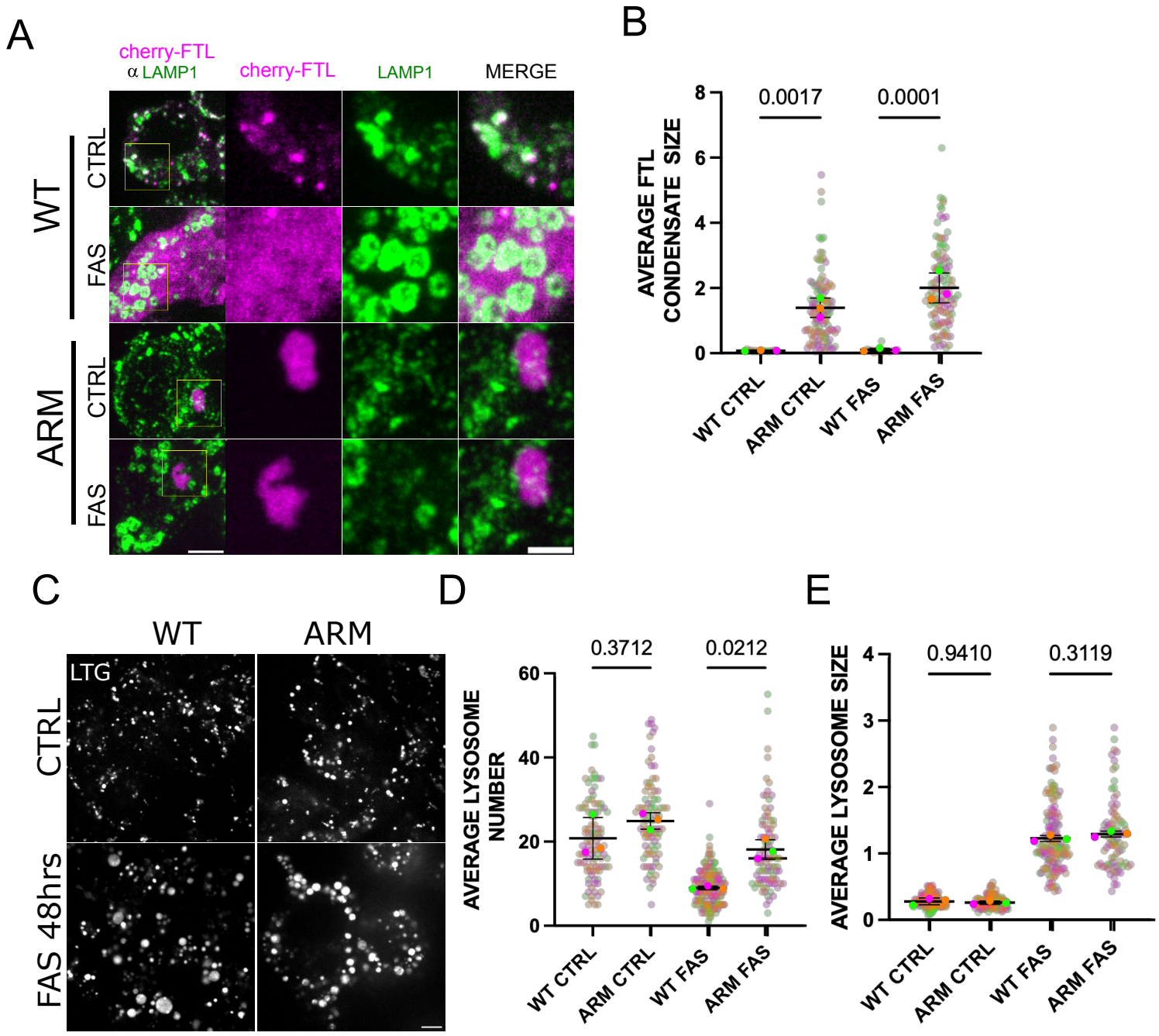

FIGURE 4

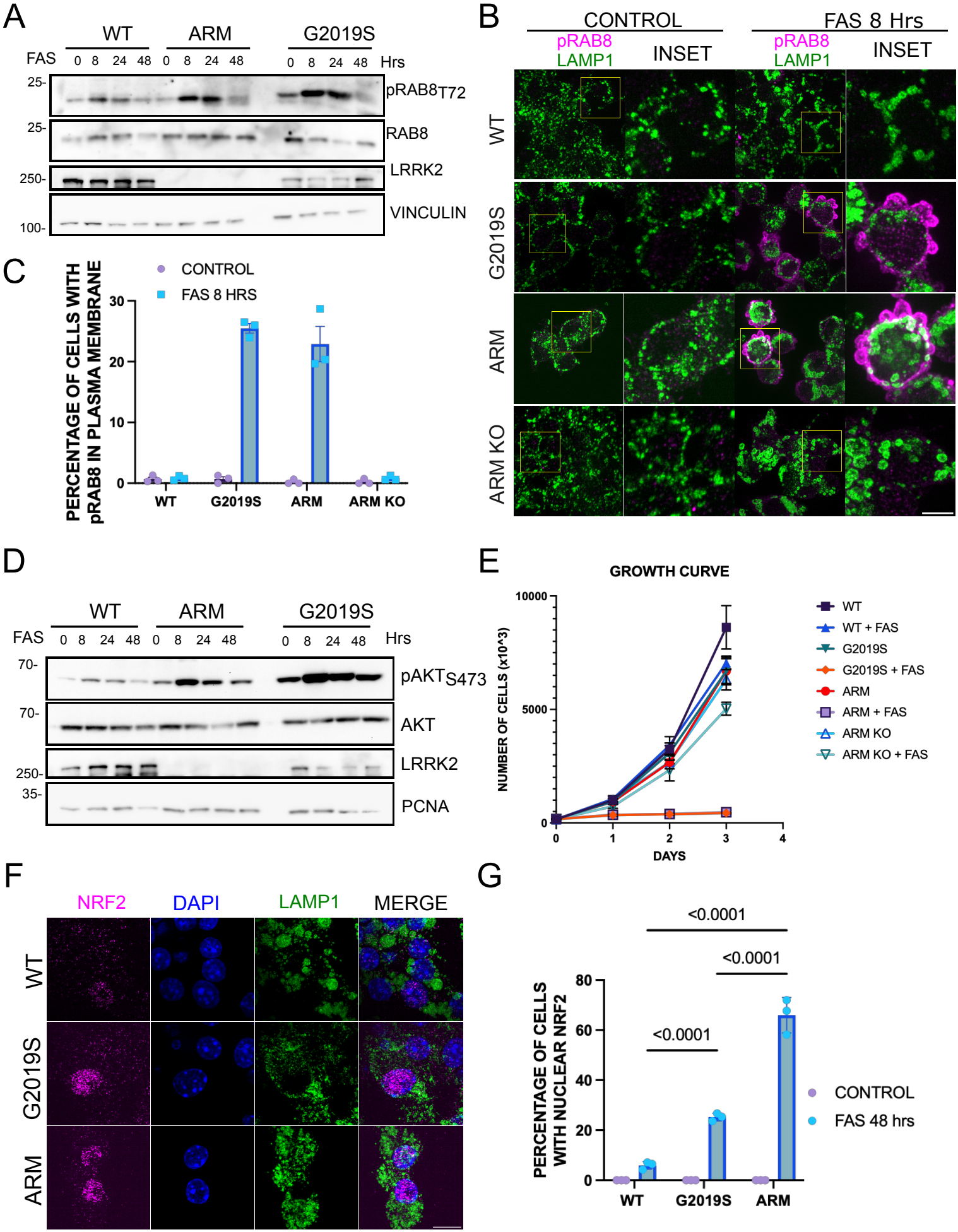
A
WT
ARM
G2019S
FAS
0 8 24 48 0 8 24 48 0 8 24 48 Hrs
25-
25-
250-
100-
pRAB8T72
RAB8
LRRK2
VINCULIN
B
CONTROL
FAS 8 Hrs
pRAB8
LAMP1
INSET
WT
G2019S
ARM
ARM KO
C
CONTROL
FAS 8 HRS
PERCENTAGE OF CELLS WITH pRAB8 IN PLASMA MEMBRANE
30
20
10
0
WT
G2019S
ARM
ARM KO
D
WT
ARM
G2019S
FAS
0 8 24 48 0 8 24 48 0 8 24 48 Hrs
70-
70-
250-
35-
pAKTS473
AKT
LRRK2
PCNA
E
GROWTH CURVE
NUMBER OF CELLS (x10^3)
10000
5000
0
0
1
2
3
4
DAYS
WT
WT + FAS
G2019S
G2019S + FAS
ARM
ARM + FAS
ARM KO
ARM KO + FAS
F
NRF2
DAPI
LAMP1
MERGE
WT
G2019S
ARM
G
<0.0001
<0.0001
<0.0001
PERCENTAGE OF CELLS WITH NUCLEAR NRF2
80
60
40
20
0
WT
G2019S
ARM
CONTROL
FAS 48 hrs
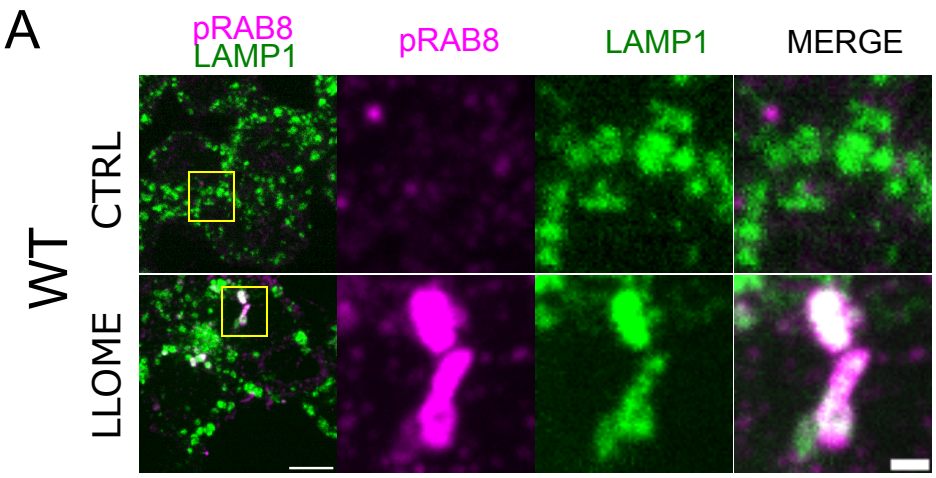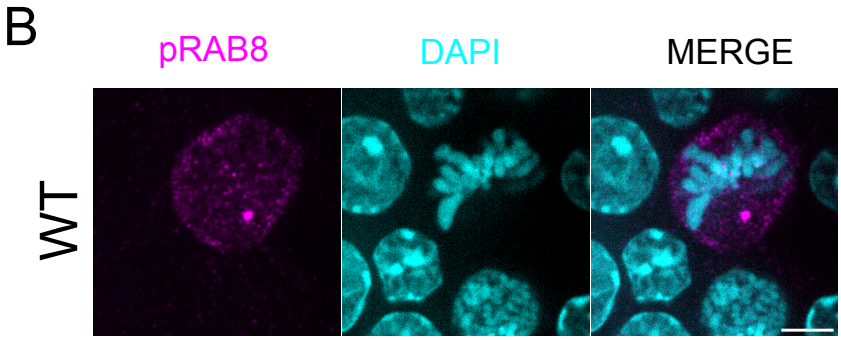
SUPPLEMENTARY FIG 4